



**HAL**  
open science

# Biological Image Segmentation Using Region-Scalable Fitting Energy with B-Spline Level Set Implementation and Watershed

R. Rahali, N. Dridi, Y. Ben Salem, Xavier Descombes, Eric Debreuve, F. de Graeve, H. Dahman

► **To cite this version:**

R. Rahali, N. Dridi, Y. Ben Salem, Xavier Descombes, Eric Debreuve, et al.. Biological Image Segmentation Using Region-Scalable Fitting Energy with B-Spline Level Set Implementation and Watershed. Innovation and Research in BioMedical engineering, 2022, 10.1016/j.irbm.2022.02.005 . hal-03866933

**HAL Id: hal-03866933**

**<https://hal.science/hal-03866933v1>**

Submitted on 23 Nov 2022

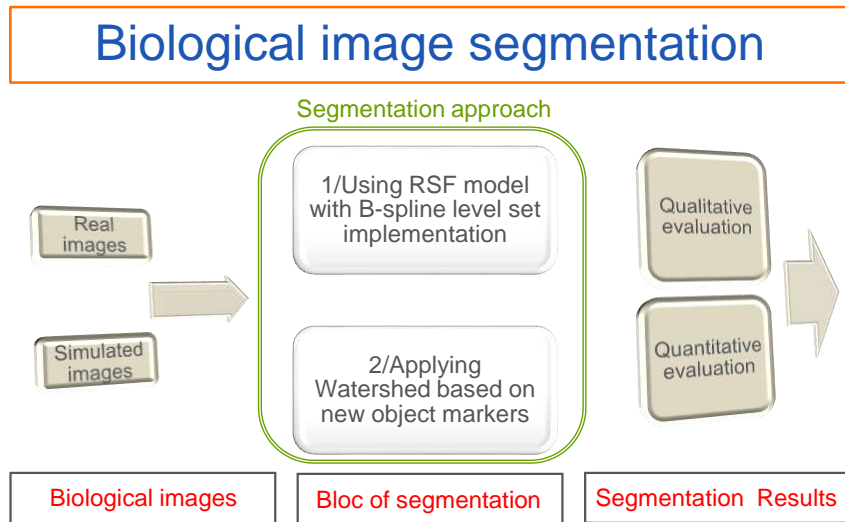
**HAL** is a multi-disciplinary open access archive for the deposit and dissemination of scientific research documents, whether they are published or not. The documents may come from teaching and research institutions in France or abroad, or from public or private research centers.

L'archive ouverte pluridisciplinaire **HAL**, est destinée au dépôt et à la diffusion de documents scientifiques de niveau recherche, publiés ou non, émanant des établissements d'enseignement et de recherche français ou étrangers, des laboratoires publics ou privés.

## Graphical Abstract

### Biological image segmentation using Region-Scalable Fitting Energy with B-spline level set implementation and Watershed

Rim Rahali, Noura Dridi, Yassine Ben Salem, Xavier Descombes, Eric Debreuve, Fabienne De Graeve, Hassen Dahman



## Highlights

### **Biological image segmentation using Region-Scalable Fitting Energy with B-spline level set implementation and Watershed**

Rim Rahali, Noura Dridi, Yassine Ben Salem, Xavier Descombes, Eric Debreuve, Fabienne De Graeve, Hassen Dahman

- New segmentation deals with intensity inhomogeneity within biological images.
- Use of continuous formulation of B-spline level set with RSF active contour model.
- Use of Watershed algorithm with a relevant choice of object markers.
- The efficiency is proved in terms of qualitative and quantitative evaluation.

# Biological image segmentation using Region-Scalable Fitting Energy with B-spline level set implementation and Watershed

Rim Rahali<sup>a,\*</sup>, Noura Dridi<sup>b</sup>, Yassine Ben Salem<sup>a</sup>, Xavier Descombes<sup>c</sup>, Eric Debreuve<sup>d</sup>, Fabienne De Graeve<sup>e</sup> and Hassen Dahman<sup>f,1</sup>

<sup>a</sup>MACS Research Laboratory-LR16ES22, National Engineering School of Gabes, Gabes University, Tunisia

<sup>b</sup>IResCoMath Research Laboratory, National Engineering School of Gabes, Gabes University, Tunisia

<sup>c</sup>Côte d'Azur University, CNRS, I3S, INRIA, Sophia Antipolis, France

<sup>d</sup>Côte d'Azur University, CNRS, INRIA, I3S, Sophia Antipolis, France

<sup>e</sup>Côte d'Azur University, CNRS, Inserm, Valrose institute of Biology, Nice, France

<sup>f</sup>LaPhyMNE Research Laboratory-LR05ES14, FSG, Gabes University, Tunisia. <sup>1</sup>Department of Electrical Engineering, National Engineering School of Gabes, Gabes University, Tunisia

## ARTICLE INFO

### Keywords:

Segmentation

RSF model

B-spline level set

Watershed

Intensity inhomogeneity

Biological image

## ABSTRACT

**Objectives** Image segmentation plays an important role in the analysis and understanding of the cellular process. However, this task becomes difficult when there is intensity inhomogeneity between regions, and it is more challenging in the presence of the noise and clustered cells. The goal of the paper is propose an image segmentation framework that tackles the above cited problems.

**Material and methods** A new method composed of two steps is proposed: First, segment the image using B-spline level set with Region-Scalable Fitting (RSF) active contour model, second apply the Watershed algorithm based on new object markers to refine the segmentation and separate clustered cells. The major contributions of the paper are: 1) Use of a continuous formulation of the level set in the B-spline basis, 2) Develop the energy function and its derivative by introducing the RSF model to deal with intensity inhomogeneity, 3) For the Watershed, propose a relevant choice of markers that considers the cell properties.

**Results** Experimental results are performed on widely used synthetic images, in addition to simulated and real biological images, without and with additive noise. They attest the high quality of segmentation of the proposed method in terms of quantitative and qualitative evaluation.

**Conclusion** The proposed method is able to tackle many difficulties at the same time: overlapped intensities, noise, different cell sizes and clustered cells. It provides an efficient tool for image segmentation especially biological ones.

## 1. Introduction

Image segmentation is a key issue in computer vision and image analysis. For biological/medical images, it is notoriously difficult due to the characteristics of images: Different scale levels, presence of clustered components, speckle and intensity inhomogeneity between pixels. For example, for medical images such as X-ray and magnetic resonance (MR) images, the inhomogeneity arises from a non-uniform magnetic field produced by radio-frequency coils as well as from object sensitivity [1]. The same is true for the UltraSound (US) B-mode images where the inhomogeneity may be originated from non-uniform beam attenuation within the body [2]. Biological images obtained in image based high throughout genome-wide RNAi screens can also be subject to intensity inhomogeneity [3]. They are carried out to study the density and the repartition of cytoplasmic RiboNucleoProtein (RNP) granules in high-throughput screening [4]. When there is a high contrast between cells and background, segmentation can be performed by image thresholding [3, 5]. In [6], DNA nuclei are segmented using DNA channel information. Fuzzy c-means based segmentation and sharpening are employed to extract cells while Voronoi diagrams are used to correct errors

due to the overlapping cells. The authors in [3] proposed an algorithm initiated by image preprocessing to reduce noise and correct out of focus degradation. Three channels are considered: DNA, F-actin and GFP-Rac. DNA channel is used for nuclei segmentation, based on a thresholding algorithm proposed by [7]. F-actin and GFP-Rac channels are used for cytoplasm segmentation. However, the thresholding technique is not able to segment clustered cell and fails with inhomogeneous images. Indeed, a fixed threshold in a given region cannot match in other region due to the difference of intensity. A common alternative to image thresholding is the Watershed algorithm, introduced in [4] for Drosophila cell segmentation. The major drawback of the Watershed is oversegmentation [8]. A more robust family of approaches was proposed, based on an active contour model that can be categorized into two classes: Edge-based models [9, 10] and region-based models [11, 12]. Edge-based models use local edge information to attract the active contour toward the object boundaries. On the other hand, region-based models aim to identify each region of interest by a region descriptor to guide the motion of the active contour. Region-based models are efficient for the segmentation of images with weak object boundaries. Two main models are used: On one hand, the Chan-Vese model [13], a special case of the Mumford-Shah (MS) functional [14].

\*Corresponding author, e-mail: rim.rahali@enig.rnu.tn  
ORCID(s): 0000-0002-5908-3002 (R. Rahali)

The image is segmented by means of the piecewise constant. On the other hand, the RSF model, proposed by authors in [15, 16], allows the use of intensity information in regions at a controllable scale, from small neighborhoods to the entire domain. Recently, the authors in [17] proposed a new model using Global Inhomogeneous Intensity Clustering. The idea is to estimate the bias field produced by the intensity inhomogeneity in the image. However, the above cited models are based on discrete level set implementation that requires a periodical re-initialization step to reshape the contour, thus increasing the computational implementation cost. An algorithm based on B-spline formulation was proposed in [18] as an alternative to the discrete level set representation. The authors proposed a continuous formulation of the level set function. The B-spline is a linear filtering method for a fast evolution of deformable models. The B-spline formulation provides global control over the entire computational domain of the level set. The minimization of the functional energy is performed with regard to B-spline coefficient. In [19], we proposed to apply the B-spline level set [18] to Drosophila cells. While the algorithm provides better performance than the discrete level set, it cannot deal with the intensity inhomogeneity. The formulation is based on the Chan-Vese model that separates the image into regions with a piecewise-constant intensity. Real images especially biological ones usually present overlaps between the ranges of intensities in the regions to segment which is challenging. Therefore, choosing an active contour model that takes into account intensity variations is a real need. In this paper, we propose to combine the advantages of both methods in [15] and [18]. A new formulation of biological image segmentation using the B-spline is proposed to take profit from the continuous formulation. Moreover, to consider the intensity inhomogeneity within the image, the RSF model is introduced. Cell segmentation consists in minimizing the energy functional with regard to the B-spline coefficients. A full framework to calculate and minimize the energy function is provided. All required equations are written and reformulated as computationally efficient convolution product. Furthermore, the method includes a Watershed step to improve the segmentation quality and to deal with artifacts. The Watershed is widely used for medical/biological images [20, 21]. In this paper, relevant object markers based on image properties are constructed using the Obj.MPP software [22]. While the primary goal of this paper is the segmentation of biological images, a particular interest is dedicated to images containing transfected<sup>1</sup> Drosophila cells. Segmentation of such images can be a difficult task due to: 1) Presence of nonhomogeneous regions 2) Shapes are always not convex (spiky and ruffly cells), 3) Cells can form clusters with weak borders which complicate their separation. To the best of our knowledge, no previous works have introduced the B-spline level set formulation with the RSF model for biological image segmentation. The contribution of this paper encompasses general biological image segmentation issues, and the special case of images containing transfected Drosophila cells. The RSF model is

applied with B-spline level set implementation, to deal with intensity inhomogeneity, followed by a Watershed step to refine the detected contours. The method is evaluated on both simulated and real images, for noisy and noiseless images. Regarding the focus of the paper, results are reported only for biological images, nevertheless the method can be applied to other types of images. Moreover, as attested in the simulation results, for Drosophila cells, the algorithm manages all the above cited difficulties.

The paper is structured as follows: Section 2, presents the problem formulation. The proposed algorithm is described in Section 3 including the segmentation functional, the minimization algorithm, and the Watershed RSF. Results on real and simulated images are provided in section 4. Finally, we conclude the paper in section 5.

## 2. Problem formulation

Let  $\Omega \subset \mathcal{R}^d$  be the image domain,  $f: \Omega \rightarrow \mathcal{R}^d$  a given d-dimensional image. Using level set formulation, the evolving interface  $C \subset \mathcal{R}^d$  is represented as the zero level set of a Lipschitz-continuous function  $\phi$  of dimension  $d + 1$  that satisfies:

$$\phi(x) > 0 \quad \forall x \in \Omega_{in} \quad (1)$$

$$\phi(x) < 0 \quad \forall x \in \Omega_{out} \quad (2)$$

$$\phi(x) = 0 \quad \forall x \in C \quad (3)$$

where  $\Omega_{in}$  and  $\Omega_{out}$  denote respectively the inside and the outside region delimited by the contour zone  $C$ . The goal of image segmentation is to distinguish the object from the image background. This problem is classically handled using the level set evolution [23]. The general form of the functional energy that drives the level set is formulated as :

$$\begin{aligned} J(\phi) = & v_{in} \int_{\Omega} g_{in}(x, \phi(x)) H(\phi(x)) dx_1 \dots dx_d \\ & + v_{out} \int_{\Omega} g_{out}(x, \phi(x)) (1 - H(\phi(x))) dx_1 \dots dx_d \\ & + v_c \int_{\Omega} g_c(x, \phi(x)) \delta(\phi(x)) \|\nabla \phi(x)\| dx_1 \dots dx_d \end{aligned} \quad (4)$$

The first and second terms refer to the energy criterion attached to the inside and outside regions defined by the contour. The last term denotes the energy criterion attached to the contour  $C$ . The function  $g_{in}(\cdot)$  and  $g_{out}(\cdot)$  describe the object and background regions,  $g_c(\cdot)$  refers to the contour.  $H$  and  $\delta$  are respectively the Heavyside and the dirac functions.  $v_{in}, v_{out}$  and  $v_c$  are constant positive hyperparameters, and  $x$  denotes the pixel. Image segmentation approaches, based on level set formulation, differ in how to define the energy functional  $J$ , the level set  $\phi$  and the algorithm used to minimise  $J$ . Two main families of methods are disguised depending on the energy functional: The Chan-Vese model [12], and the RSF one [15, 24]. Those based on the Chan-Vese model are formulated using discrete representation of the level set [25, 26, 27]. As alternative, continuous

<sup>1</sup>Transfection: is the process of artificially introducing nucleic acids (DNA or RNA) into cells. Such modification of foreign nucleic acid lead to a change of the properties of the cell, allowing the study of gene function and protein expression in the context of the cell.

formulation of the level set function was proposed in [18] where the level set is defined as a continuous parametric function using the B-spline. The minimization of the energy functional is performed with regards to the B-spline coefficients. As described in [18], each step is considered as a filtering operation with a B-spline kernel. The gradient descent method is used to perform energy function minimization. The Chan-Vese model presents a limit: The image intensity is approximated by a constant inside and outside contour. Therefore, the method is not suitable for images with intensity inhomogeneity. The latter occurs in many real images of different modalities, as is often the case for medical and biological images [3, 28]. To address this problem, the authors in [15, 24] proposed the RSF active contour model. This model uses intensity information in local regions at a controllable scale [15]. Two fitting functions  $f_{in}(x)$  and  $f_{out}(x)$  to locally approximate the intensities inside and outside the contour were introduced. The energy functional is given by:

$$J(C, f_{in}, f_{out}) = v_{in} \int \left[ \int_{\Omega_{in}} K_{\sigma}(x-y) |I(y) - f_{in}(x)|^2 dy \right] dx + v_{out} \int \left[ \int_{\Omega_{out}} K_{\sigma}(x-y) |I(y) - f_{out}(x)|^2 dy \right] dx + v_c \int |\nabla H(\phi(x))| dx \quad (5)$$

$C$  is a closed contour that separates the image domain into two regions inside ( $C$ ) and outside ( $C$ ). The last term in Eq.5 is the regularization term. To relate with previous notation in Eq.4, note here that  $d=2$  and  $(x_1, x_2)=(x, y)$ . When comparing the model given in Eq.5 with the Chan-Vese model [18], the two constants  $\mu_{in}$  and  $\mu_{out}$  are replaced by two spatially varying fitting functions  $f_{in}(x)$  and  $f_{out}(x)$ . Besides, the energy in regions inside and outside the contour are weighted by a kernel  $K$ .  $K$  is a non-negative and satisfies three conditions: 1)  $K$  should be symmetric, 2)  $K(u) \geq K(v)$ , if  $|u| < |v|$  and  $\lim_{|u| \rightarrow \infty} K(u) = 0$  (called localization property), 3) The integral over the entire space is equal to 1.  $K$  controls the size of the effective evolved energy in each region. In [15], the Gaussian kernel is chosen :

$$K_{\sigma}(x) = \frac{1}{\sqrt{(2\pi)\sigma}} e^{-|x|^2/2\sigma^2} \quad (6)$$

where  $\sigma$  is a constant to control the local region size.  $\sigma$  should be chosen carefully since the larger the bandwidth is, the more likely it is to result in a fuzzy boundary. However, smaller bandwidth can not characterize the local image information and results in redundant contours. Due to the localization property of the Gaussian kernel, the contribution of the intensity  $I(y)$  to the RSF energy decreases to zero as the pixel  $y$  moves away from the pixel center  $x$ . This property plays a key role in segmenting images with intensity inhomogeneity. The energy functional in Eq.5 is minimized using the descent gradient algorithm, primarily with respect to  $f_{in}$  and  $f_{out}$ , for fixed  $\phi$ , then with regard to  $\phi$  keeping  $f_{in}$  and  $f_{out}$  constants [18].

### 3. Proposed method: RSF model with B-spline level set implementation and Watershed

A new method is proposed for image segmentation based on B-spline level set implementation with the RSF model followed by a Watershed step. Considering the RSF model instead of the Chan-Vese makes it possible to deal with the intensity inhomogeneity within the image. Besides, the Watershed improves the segmentation results obtained with the B-spline level set, and it is particularly efficient to carry out on the clustered cells. In this section, a detailed description of the segmentation functional, the minimization algorithm, and the Watershed RSF are provided. The section is ended with a graphical description of the proposed method.

#### 3.1. Segmentation functional

In [15], the authors used a narrow-band implementation that limits the control over the conventional level set domain. As an alternative, in [18] the B-spline formulation was suggested to provide global control over the entire computational domain of the level set. However, the functional energy was defined as in the Chan-Vese model [12], where the image intensity is supposed to be constant inside and outside the contour. The constants are respectively equal to the average of the intensities in the region inside and outside contour, which do not contain any local information. Therefore, poor performance was obtained especially for images with intensity inhomogeneity, such as biological images [3].

To tackle this problem, we introduce a novel method that profits from the advantages of both the RSF model and the framework of [18]. A new formulation of the energy functional based on the B-spline is established. Moreover, to deal with the intensity inhomogeneity, the image intensities inside and outside the contour are no longer considered as constant. They are replaced by functions that depend on local region information as in [15]. Using the same notation as in the previous section, the energy functional  $J$  is given by :

$$J(\phi, f_{in}, f_{out}) = v_{in} \int_{\Omega} \left[ \int_{\Omega} K_{\sigma}(x-y) |I(y) - f_{in}(x)|^2 H(\phi(y)) dy \right] dx + v_{out} \int_{\Omega} \left[ \int_{\Omega} K_{\sigma}(x-y) |I(y) - f_{out}(x)|^2 (1 - H(\phi(y))) dy \right] dx + v_c \int_{\Omega} \delta(\phi(x)) |\nabla \phi(x)| dx \quad (7)$$

In practice, the Heaviside function  $H$  and the Dirac function  $\delta$  in the above energy functional can be replaced with the following regularized expressions :

$$\begin{cases} H_{\epsilon}(x) = \frac{1}{2} + \frac{1}{\pi} \arctan\left(\frac{x}{\epsilon}\right) \\ \delta_{\epsilon}(x) = \frac{d}{dx} H_{\epsilon}(x) \end{cases} \quad (8)$$

where  $\varepsilon$  is a real positive constant. By replacing  $H$  and  $\delta$  with Eq.8, the energy functional in Eq.7 equals to :

$$\begin{aligned} J(\phi, f_{in}, f_{out}) = & \\ & v_{in} \int_{\Omega} \left[ \int_{\Omega} K_{\sigma}(x-y) |I(y) - f_{in}(x)|^2 H_{\varepsilon}(\phi(y)) dy \right] dx \\ & + v_{out} \int_{\Omega} \left[ \int_{\Omega} K_{\sigma}(x-y) |I(y) - f_{out}(x)|^2 (1 - H_{\varepsilon}(\phi(y))) dy \right] dx \\ & + v_c \int_{\Omega} \delta_{\varepsilon}(\phi(x)) |\nabla \phi(x)| dx \end{aligned} \quad (9)$$

The first term corresponds to the energy of the region inside the contour, denoted  $J_{in}(\phi, f_{in})$ . The second term represents the energy of the region outside the contour named  $J_{out}(\phi, f_{out})$ . The last term refers to the regularisation term. The expression given in Eq.9 is developed in Appendix A, we demonstrate that the energy function can be written as convolution product that yields computationally efficient implementation.

### 3.2. Minimization algorithm

The splines are piecewise polynomials with pieces that are smoothly connected together, the joining points of the polynomials are called knots. The Basis splines (B-splines) are symmetrical, bell-shaped functions constructed from the  $(n+1)$ -fold convolution of a rectangular pulse [29]. A spline function can be uniquely represented as linear combination of the B-splines [30]. Here, we propose to use B-spline representation of the level set function  $\phi(x)$  [29] :

$$\phi(x) = \sum_{k \in \mathbb{Z}^d} c[k] \beta^n\left(\frac{x}{h} - k\right) \quad (10)$$

where  $\beta^n(\cdot)$  is the uniform symmetric  $d$  dimensional basic building blocks for splines of degree  $n$ .  $\beta^n(\cdot)$  is a separable function and can be written as:

$$\beta^n(x) = \prod_{j=1}^d \beta^{(n)}(x_j) \quad (11)$$

where  $\beta^{(n)}(x_j)$  is a one dimensional B-splines. The separability property is important, it is used to formulate the gradient as a sequence of simple 1D convolution.  $n$  is the degree of a spline, i.e. the degree of the polynomial defining each segment.  $h$  represents the regular spacing between the knots of splines located on a grid spanning  $\Omega$  and  $c[k]$  are the coefficients of the B-spline representation. The minimization of the energy functional is performed, with respect to the B-spline coefficients  $c[k]$ . This requires the calculation of the derivative of Eq.(9), developed in Appendix B and it leads to :

$$\begin{aligned} \frac{\partial J}{\partial c[k]} = & \int_{\Omega} \left[ \tilde{w}(y) \beta^n\left(\frac{y}{h} - k\right) \right] dy \\ & - v_c \int_{\Omega} w_c(y) \beta^n\left(\frac{y}{h} - k\right) dy \end{aligned} \quad (12)$$

with,

$$\begin{aligned} \tilde{w}(y) = & \int_{\Omega} K_{\sigma}(x-y) v_{in} |I(y) - f_{in}(x)|^2 \delta_{\varepsilon}(\phi(y)) dx \\ & - \int_{\Omega} K_{\sigma}(x-y) v_{out} |I(y) - f_{out}(x)|^2 \delta_{\varepsilon}(\phi(y)) dx \end{aligned} \quad (13)$$

and

$$w_c(y) = \text{div} \left( \frac{\nabla \phi(y)}{\|\nabla \phi(y)\|} \right) \delta_{\varepsilon}(\phi(y)) \quad (14)$$

Note here that the major difference with the algorithm proposed in [18] is the presence of the integral over  $x$  in the term  $\tilde{w}(y)$ . Besides,  $f_{in}$  and  $f_{out}$  are not constant and depend on pixel  $x$ . Such formulation allows the inclusion of local information of the inside and the outside region of the contour, which is crucial for an image with intensity inhomogeneity.

The second term in Eq.12 is the regularization term, it plays the role of smoothing the zero level set to maintain the regularity of the contour. Without the regularization term,  $\phi$  grows to very large values on both sides of the zero level set. Then,  $\delta_{\varepsilon}(\phi)$  in Eq.14 takes an arbitrarily small value, making the motion of the contour slower and can even be stopped before it reaches the desired object boundaries. The analytical resolution of the energy minimization criterion with respect to the B-spline coefficients is not tractable, therefore a numerical algorithm is required. Here, the gradient descent method is applied, the  $i^{th}$  iteration of the algorithm is given by :

$$c^{(i+1)} = c^{(i)} - \lambda \nabla_c J(c^{(i)}) \quad (15)$$

where  $\lambda$  is the iteration step and  $\nabla_c$  corresponds to the gradient of the energy relative to the B-spline coefficients, obtained from Eqs.12, 13 and 14. Moreover, in order to get tractable form of the energy gradient, Eq.12 is written as :

$$\nabla_c J = \frac{\partial J}{\partial c[k]} = \psi \otimes b_h^n[k] \quad (16)$$

$\otimes$  is the convolution product,  $\tilde{w}$  given in Eq.13, equals to:

$$\tilde{w} = \tilde{w}_1 + \tilde{w}_2 + \tilde{w}_3 \quad (17)$$

where

$$\tilde{w}_1 = I^2(y) (v_{in} - v_{out}) \delta_{\varepsilon}(\phi(y)) \quad (18)$$

$$\tilde{w}_2 = 2I(y) \left[ K_{\sigma} \otimes (v_{out} f_{out} - v_{in} f_{in}) \right] \delta_{\varepsilon}(\phi(y)) \quad (19)$$

$$\tilde{w}_3 = \left[ K_{\sigma} \otimes (v_{in} f_{in}^2 - v_{out} f_{out}^2) \right] \delta_{\varepsilon}(\phi(y)) \quad (20)$$

Demonstration of the above results is provided in appendix B. It is noteworthy to mention that writing the gradient as a convolution product allows an efficient implementation of the algorithm.

### 3.3. Importance of B-spline formulation

As given in Eq.10 the level set function is modelled as a continuous parametric function expressed on a B-spline basis. This is different from the discrete representation commonly used with the level set based approaches. In fact, the B-splines provide better approximation of complex shapes to be easy to manipulate (derivative calculation, separable function,...). More details about the advantages of such formulation and a list of primary applications are

provided in [29]. Recently, the authors in [31] proposed several methods to improve the efficiency and accuracy of B-spline based methods for different applications. Furthermore, as detailed in the previous section, image segmentation is based on the minimization of the energy functional performed using the gradient descent algorithm. The gradient may be steep or flat leading to inaccuracies in the numerical approximation [25]. Classically, this is handled by reshaping the level set through periodical re-initialization of the level-set function as the signed distance function to the zero level [25]. However, this introduces problems like when and how the re-initialization should be performed in addition to the numerical accuracy perturbation. Besides, the level set becomes topologically less flexible, since it prevents the level set to develop new contours (i.e., new zero-level components) [25]. By using the B-spline formulation, this step may be avoided by normalizing the B-splines parameters to provide natural bound to the level set function [18]. Moreover, since the minimization of the energy functional is performed with regards to B-spline coefficients, as shown in the previous section, each step is performed as sequence of simple 1D convolutions, which is computationally efficient. In our previous work [19], two methods were compared with and without the B-spline representation, for both, the Chan-Vese model is used for image approximation. Results attest the gain of performance obtained with the B-spline formulation. Nevertheless, performance are limited in the presence of intensity inhomogeneity, tackled in this paper. Finally, recall to the major difference with [18], is the use of RSF model to approximate the image instead of Chan-Vese to deal with intensity inhomogeneity. Besides, in this work we propose to include the Watershed step detailed in next section.

### 3.4. Watershed RSF

The Watershed algorithm is largely used for image segmentation [20, 32]. From local minima [33], the Watershed finds the crest lines in the image by the simulation of the flooding process [34]. Considering all local minima leads to an oversegmented image and makes the segmentation result unusable. To tackle this issue, markers of relevant regions in the image are employed to reduce the number of local minima and refine the segmentation. The Watershed floods from markers instead of flooding from all local minima. The Watershed algorithm takes as input the segmentation result of the RSF model with B-spline level set implementation. Then three steps are performed: First, compute the distance map of the input image, which consists of an Euclidean distance measure between each pixel of the object and its nearest zero pixel that touches the object border. Then, a Gaussian filter is applied to the distance map. Second, select the object markers using the Obj.MPP software <sup>2</sup>. The Obj.MPP [22] includes prior information about cells of interest. Third, apply the Watershed to local minima from the reverse filtered distance map, these local minima belong to object markers. The Obj.MPP software is based on the Marked Point Process (MPP) [35], it consists in the

detection of parametric objects in the image using two main criteria: The shape and the radiometry. Shapes are defined by marks that represent the parameters of the selected objects. The radiometric constraint is calculated directly through the object mean intensity measurement or indirectly through the measurement of the relative intensity of the object contour [22]. The framework fits sets of shapes on the image plane and selects the ones matching best with the predefined object characteristics. A space of marks is defined, taking into account the variability of object size and morphology. Besides, constraints on the spatial repartition of objects are embedded in the framework to control the average overlap between objects. Furthermore, a set of parameters related to the selection should be fixed consisting of: 1) The minimum value of the quality function fostering objects that fits the data, 2) The number of iterations, 3) The number of birth cells per iteration. Given the preselected set of objects, the best elements are chosen using the graph cut algorithm [36]. Three outputs are given: The file containing the raw image with objects contours highlighted and two masks for the segmented labeled objects and the sole objects contours. An example of labeled object markers for *Drosophila* cells is illustrated in Fig.1. In this paper, real and simulated biological datasets are used. For the real *Drosophila* dataset, Obj.MPP parameters are set as follows: the selected shape geometry is an ellipse, the minimum value of the quality equals 0.5, the overlapping tolerance equals 20%, the number of iterations equals 8000 and the number of birth cells per iteration equals 100. For simulated dataset, Obj.MPP parameters are set as follows: the selected shape geometry is an ellipse, the minimum value of the quality equals 0.2, the overlapping tolerance equals 0%, the number of iterations equals 8000 and the number of birth cells per iteration equals 3.

### 3.5. Graphical description of the proposed method

The proposed method is described by a graph including different blocs as shown in Fig.2. The input image is submitted to a preprocessing step, consisting of local normalization [37] and Gamma correction [38]. The latter is added to scale the range of pixel intensity. The bloc of the segmentation in Fig.2 corresponds to the RSF model with B-spline level set implementation, applied to the preprocessed image. Then, the Watershed is performed to the reverse filtered distance map of the segmentation result. The Watershed is applied to the segmentation result of the RSF bloc rather than using the image gradient or the image resulting from the threshold algorithm. For the Watershed, object markers are constructed using the Obj.MPP.

Moreover, it is worth noting that biologists are interested in segmenting ribonucleic-protein particles present in the cytoplasm of healthy cells. Therefore after the segmentation, a postprocessing step is added to refine the segmentation results based on prior information about cell status: Dead or alive, the cell's shape, and dimension. Images presenting kernels Barycenters of the living cells are used in

<sup>2</sup><https://gitlab.inria.fr/edebreu/Obj.MPP>



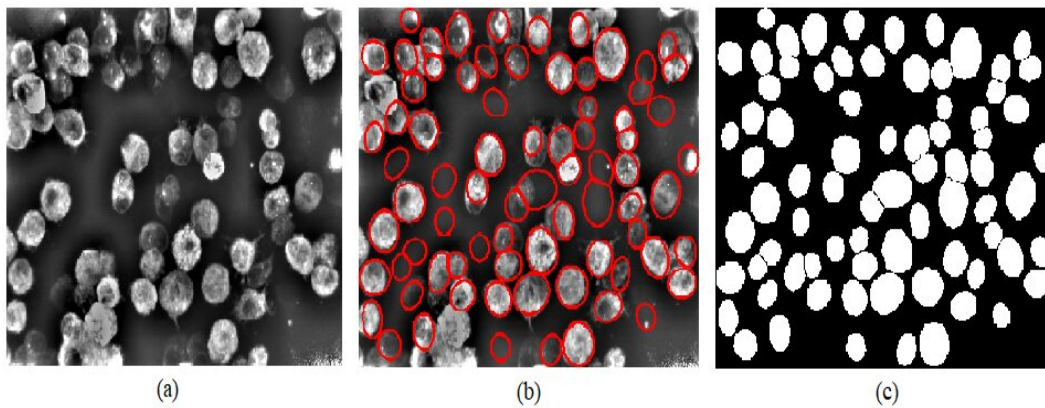


**Figure 1:** (a) Preprocessed Drosophila 1, (b) Superposition of the preprocessed image and markers (red), (c) Selected mask of markers using Obj.MPP.

the postprocessing step as filters, removing all the detected dead cells. Cells of interest are characterized by: CircuMin equals 0.6, minimum size equals 1500, maximum size equals 4000, intenMin equals 100 and intenMax equals 2000. The above-cited criteria are chosen to avoid extreme cell shapes and to be able to segment the protein of interest in the cytoplasm of healthy cells. Besides, only cells that are not touching borders are detected because the biologists need to isolate the cells in their entirety before performing statistical studies. For the rest of the paper, the proposed method is named B-spline-WatershedRSF.

#### 4. Results

The main contribution of this paper is an algorithm tackling the intensity inhomogeneity problem. Therefore, we propose, to evaluate the performance on different synthetic images widely used in the literature as typical examples of images with intensity inhomogeneity, Fig.3. For such images, simple thresholding or an algorithm assuming constant intensities in two different regions cannot segment them correctly. In addition, results are compared with the Vector Field Convolution (VFC) algorithm proposed in [39]. The authors propose to include a new external force for the active contour called VFC. The latter is obtained by the convolution of a vector field kernel with the edge map generated from the image. The code given in [40] is used. Results are presented in Fig.4. It is clear that the VFC fails to capture the boundaries of the object of interest when the image presents intensity inhomogeneity. This behaviour is expected, indeed the VFC is based on the snake model, using the global region information, assuming that the image intensity is homogeneous [12]. As illustrated in Fig.3, the proposed algorithm efficiently segments the image despite the clear presence of intensity variations between regions. The content of each image is correctly limited by the red curve indicating the final segmentation result. The main purpose of this paper is the segmentation of real biological images containing intensity inhomogeneity, in particular images containing transiently transfected

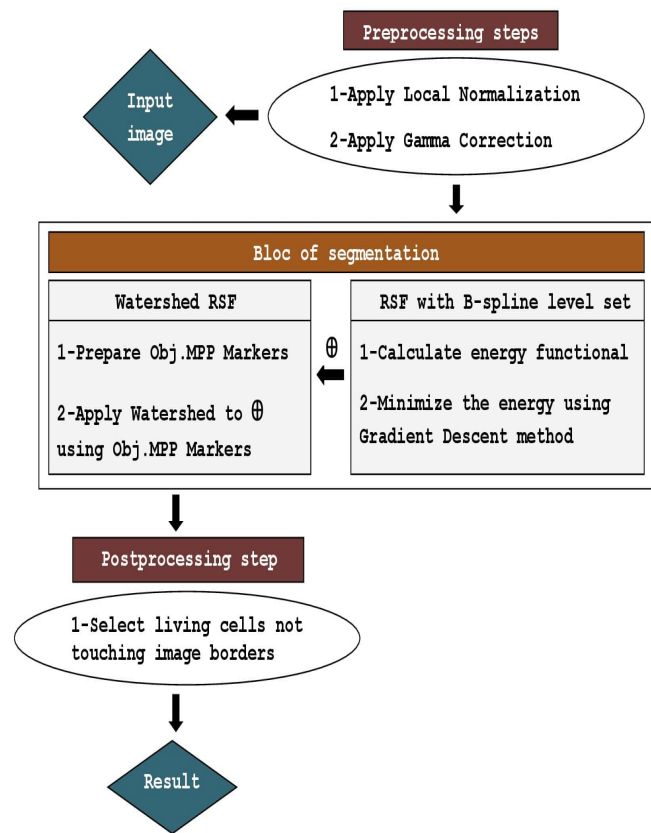


**Figure 2:** Diagram exposing the different steps of the proposed method B-spline-WatershedRSF.  $\oplus$  indicates the segmentation mask resulting from the first bloc of RSF with B-spline level set.

Drosophila S2R+ cells. Moreover, additional results on simulated images and skin lesion images are provided. More details on the datasets are given in the next section. First, the RSF model with B-spline implementation is compared with a basic thresholding algorithm. Second, performance are attested with regard to the baseline of the International Skin

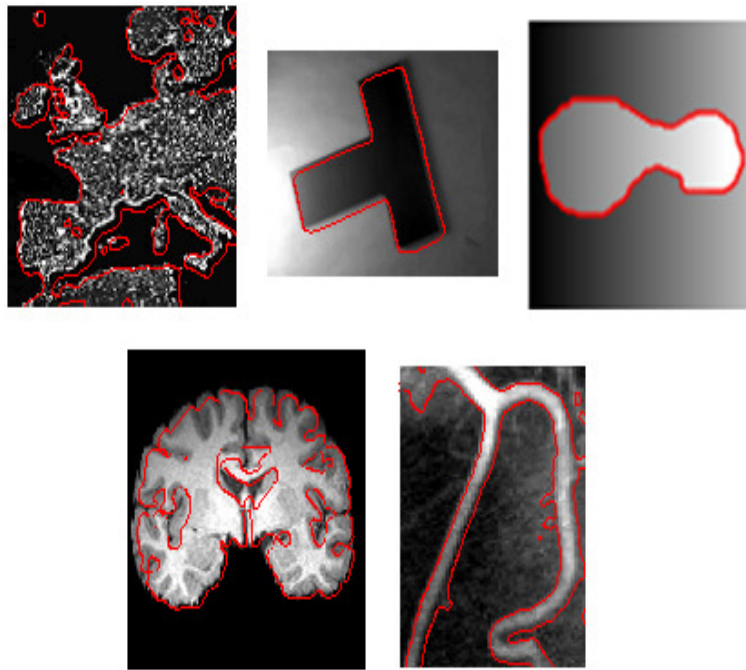


**Figure 3:** Segmentation of different synthetic images using RSF model with B-spline level set implementation.

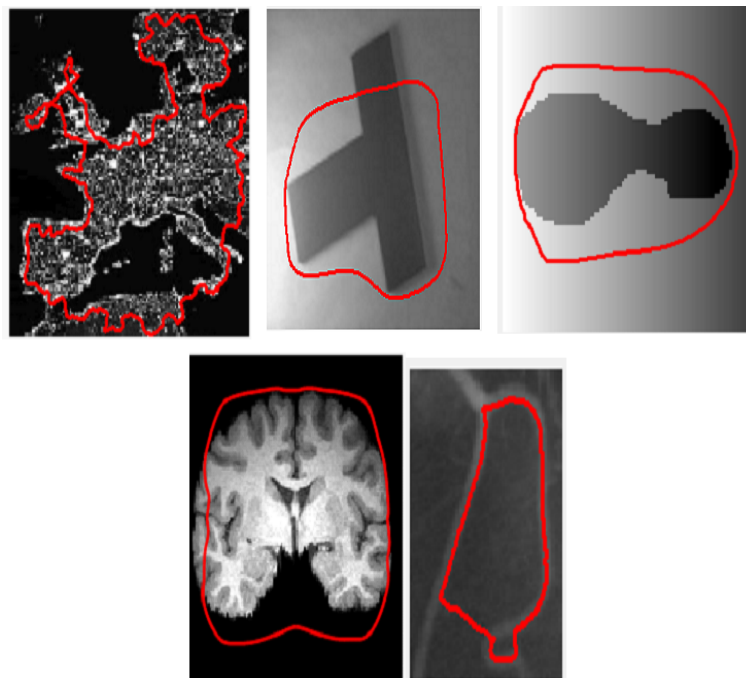


**Figure 4:** Segmentation of different synthetic images using the VFC algorithm.

Imaging Collaboration (ISIC) 2018 challenge [41]. Third, three algorithms are compared:

1. The SegWatershed algorithm, developed by Pr. Xavier Descombes<sup>3</sup>. The algorithm is based on the Watershed [34] applied to the image gradient. The segmentation is based on prior information about the objects of interest. Inscribed circles of cell kernels

2. The B-spline Chan-Vese algorithm presented in [18], based on the Chan-Vese model, i.e. without considering intensity inhomogeneity. The preprocessing consists of local normalization applied to images

containing transiently transfected *Drosophila* S2R+ cells.

3. The proposed algorithm B-spline-WatershedRSF based on the RSF model with B-spline level set implementation and the MCW. The preprocessing includes local normalization and Gamma correction, applied to images containing transiently transfected *Drosophila* S2R+ cells.

The three algorithms are followed by the same postprocessing step given in Fig.2. For all experiments using the B-spline level set implementation, the coefficients  $v_{in}$ ,  $v_{out}$  and  $v_c$  in Eq.9 equal 1, 2 and 0.05 respectively. The spacing interval  $h$  in Eq.10 equals 1 and the iteration step  $\lambda$  in Eq.15 is set to 0.5. For the RSF model, the Gaussian Kernel is applied with standard deviation  $\sigma$  equals 30. Segmentation performances of the different algorithms are evaluated based on the  $F_1$  score [42], the Jaccard index [43] and cell detection errors. The mean of the  $F_1$  score and the Jaccard index, over the set of labels of the image, is calculated. Results are represented as percentages rounded to the nearest integers. The cell detection errors are measured by the number of true positives (TP), false positives (FP), and false negatives (FN). All of these metrics are provided by the daccuracy framework<sup>4</sup>, developed by Dr. Eric Debreuve<sup>5</sup>. The framework computes the essential metrics for image segmentation.

#### 4.1. Dataset description

The proposed algorithm is evaluated using three datasets:

1. Real dataset: Provided by Dr. Fabienne De Graeve<sup>6</sup>. Images contain *Drosophila* S2R+ cells that are transiently transfected generating a heterogeneous population of cells. Not all the cells are transfected, and the ones that are transfected can be subdivided into three categories depending on the level of expression of the GFP tagged protein: high, medium, and low levels. The images are taken in the context of an RNAi screen using a high throughput confocal microscope Opera (Perkin Elmer) and a 63X water objective. The genetic contexts induce the death of some cells. Only live cells are relevant to keep in final segmentation results. The image contains  $686 \times 518$  pixels and it is named as *Drosophila i*, with  $i$  varying from 1 to 5. It is worth pointing out that the presence of clusters with variable sizes and morphologies in addition to locally low contrast pixels render the image segmentation particularly challenging.
2. Simulated dataset: Images are generated with Simcep simulator<sup>7</sup> which is implemented using object-oriented programming [44]. To generate an image, different options are given to the simulator such as cell population properties and the microscope acquisition that includes spatially variable out-of-focus

blurring, irregular illumination variations, and sensor noise. In this study, images are  $500 \times 500$  pixels and contain 30 cells. First, a limited number of dataset is considered to demonstrate the algorithm performance per image. The data include four images: Simcep 1 to Simcep 4 without clustered nor overlapping cells. On the other hand, Simcep 5 and Simcep 6 encompass several clusters and overlapping cells. Furthermore, 50 simulated images are generated, named Simcep  $i$  with  $i$  varying from 1 to 50. The mean of the  $F_1$  score and the Jaccard index are calculated to attest the algorithm performance for larger dataset. Skin lesion dataset: we apply our algorithm to 50 images of skin lesion. They belong to the validation dataset used in the ISIC challenge in 2018 [41]. The images are publicly accessible to support the development of automated melanoma diagnosis algorithms across three tasks of lesion analysis: The lesion segmentation, the attribute detection, and the disease classification. In this paper, the focus is on the first task, 50 images with different sizes are used. The dataset presents different positions and forms of the skin lesion within the image.

For the real dataset, the ground truth is provided by Dr. Fabienne De Graeve who performed the manual segmentation. For the simulated images, ground truth is given by the simulator Simcep [44]. The ground truth for the skin lesion dataset is publicly accessible in ISIC 2018 challenge [41]. Images presenting kernels Barycenters of the living cells are given by Dr. Fabienne De Graeve for the postprocessing step.

#### 4.2. RSF model with B-spline level set implementation compared to thresholding algorithm

The threshold has been widely applied in image segmentation. The basic idea of thresholding is to automatically select an optimal or several optimal gray-level thresholds to separate objects of interest in the image from the background based on their gray-level distribution. To demonstrate the relevance of using the RSF model, the proposed algorithm is compared to the Otsu algorithm [7, 45]. The goal is to evaluate the performance of the RSF with B-spline level set, therefore the Watershed bloc is not included as presented in Fig.2. The Otsu is a bi-level thresholding algorithm: Pixels with gray levels less than the threshold are assigned to the background, and the others to the foreground. It selects the global optimal threshold by maximizing the between-class variance. Segmentation results are illustrated in Fig.5 for *Drosophila* 2. Due to the limited space, results are only shown for one image, however no difference is noted for the other images in term of segmentation performance. In Fig.5, the columns (starting from the left) present respectively: The preprocessed image,

<sup>3</sup>Pr. Xavier Descombes is a professor at the University Côte d'Azur, CNRS, I3S Laboratory, INRIA, France

<sup>4</sup><https://gitlab.inria.fr/edebreu/daccuracy>

<sup>5</sup>Dr. Eric Debreuve is a permanent researcher at the University Côte d'Azur, CNRS, INRIA, I3S Laboratory, France

<sup>6</sup>Dr. Fabienne De Graeve is a lecturer at the University Côte d'Azur, IBV, CNRS, INSERM, France

<sup>7</sup><https://www.cs.tut.fi/sgn/csb/simcep/tool.html>

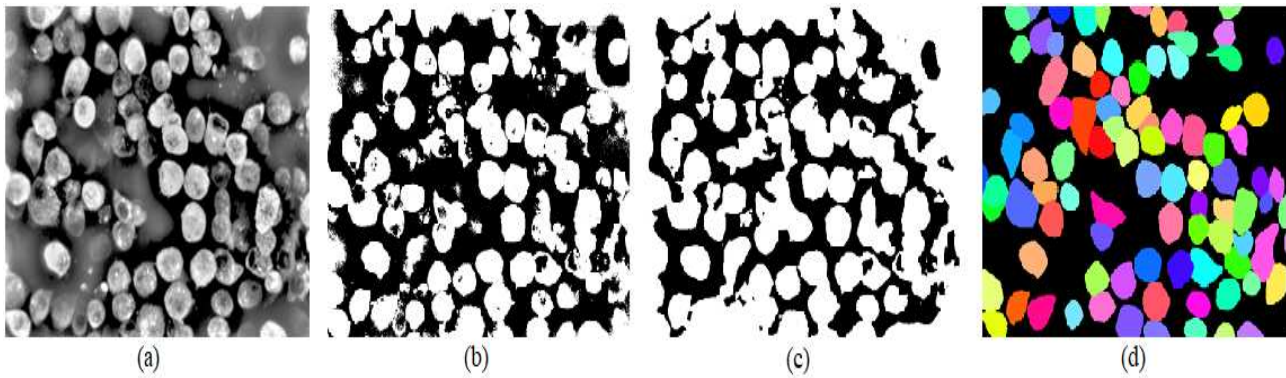


**Figure 5:** (a) Preprocessed Drosophila 2, (b) Segmentation result using the Otsu algorithm, (c) Segmentation result using the RSF algorithm and (d) Ground truth.

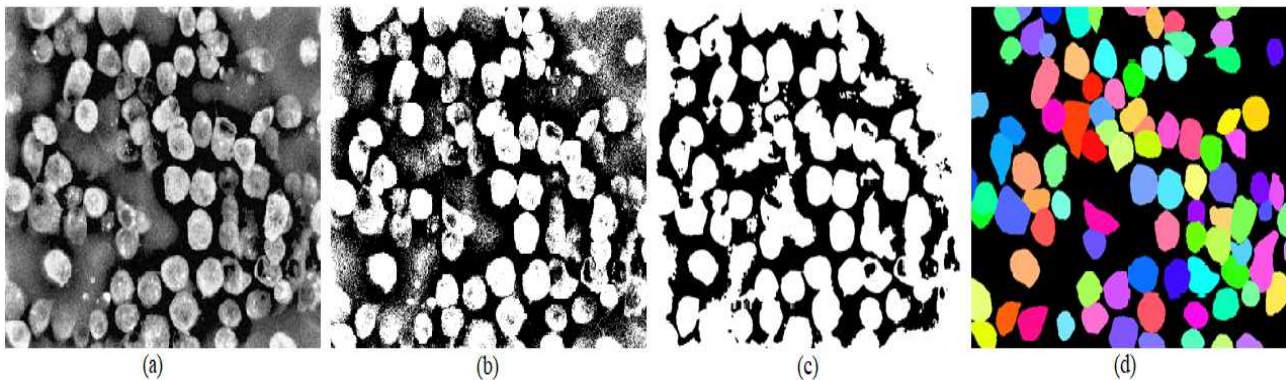


**Figure 6:** (a) Preprocessed Drosophila 2 with additive Gaussian noise (SNR=15dB), (b) Segmentation result using Otsu algorithm, (c) Segmentation result using RSF algorithm, (d) Ground truth.

segmentation result for the Otsu algorithm, segmentation result for the RSF algorithm, and the ground truth. Here, the Watershed and the postprocessing step are not applied. From observation, the number of detected cells is increased using the RSF algorithm. The Otsu algorithm confuses cells with the background. Furthermore, it is sensitive to intensity variations and the size of the target. The thresholding algorithm is suitable for images with single peak variance, not for images with intensity inhomogeneity that present multiple peak variance.

To attest the performance of the two algorithms for noisy images, segmentation results for Drosophila 2 with additive Gaussian noise are given in Fig.6. Results are obtained for Signal to Noise Ratio (SNR) equals 15dB. As observed, it is clear that the performance is degraded with the Otsu algorithm: The segmented image includes noise in the background. Moreover, the RSF algorithm is more robust to the noise: When comparing Fig.5-(c) and Fig.6-(c), segmentation performances are almost the same.

### 4.3. RSF model with B-spline level set implementation compared to ISIC 2018 baseline

As described in [41], the segmentation task in the ISIC 2018 challenge is performed using the Deep learning

approach. Specifically, an encoder and a decoder in a U-NET type structure is applied [46, 47]. In this section, we compare the results, provided by both the ISIC 2018 baseline [41] and the proposed RSF model with the B-spline level set implementation. For our algorithm, 50 skin lesion images are segmented, where the preprocessing and postprocessing steps are included. Same hyperparameters and initialization are used for the 50 images. The hyperparameters are fixed as  $v_{in}=2$ ,  $v_{out}=3$ ,  $v_c=0.5$ ,  $\lambda=0.5$ ,  $h=1$ , and  $\sigma=35$ . Moreover, a circular initialization is considered with a radius relative to the image size. For these experiments, the preprocessing consists in converting the images to gray level ones and downsizing them using a scale of 0.4. While, the artefacts, obtained after the segmentation, are eliminated by the postprocessing. Here, the Watershed is not required since the images encompass one object of interest. Indeed, the Watershed is relevant for multiple object segmentation with eventual presence of clustered ones. Examples of skin lesion segmentation are given in Fig.7. As observed, in Fig.7, the proposed algorithm is able to properly segment the skin lesion images. Although, these images do not include intensity inhomogeneity or clustered cells, the difficulty is related to the different size of the object of interest. Numerical evaluation is given in Table.1, using the Jaccard index. Note, that, to get fair comparison, the latter index

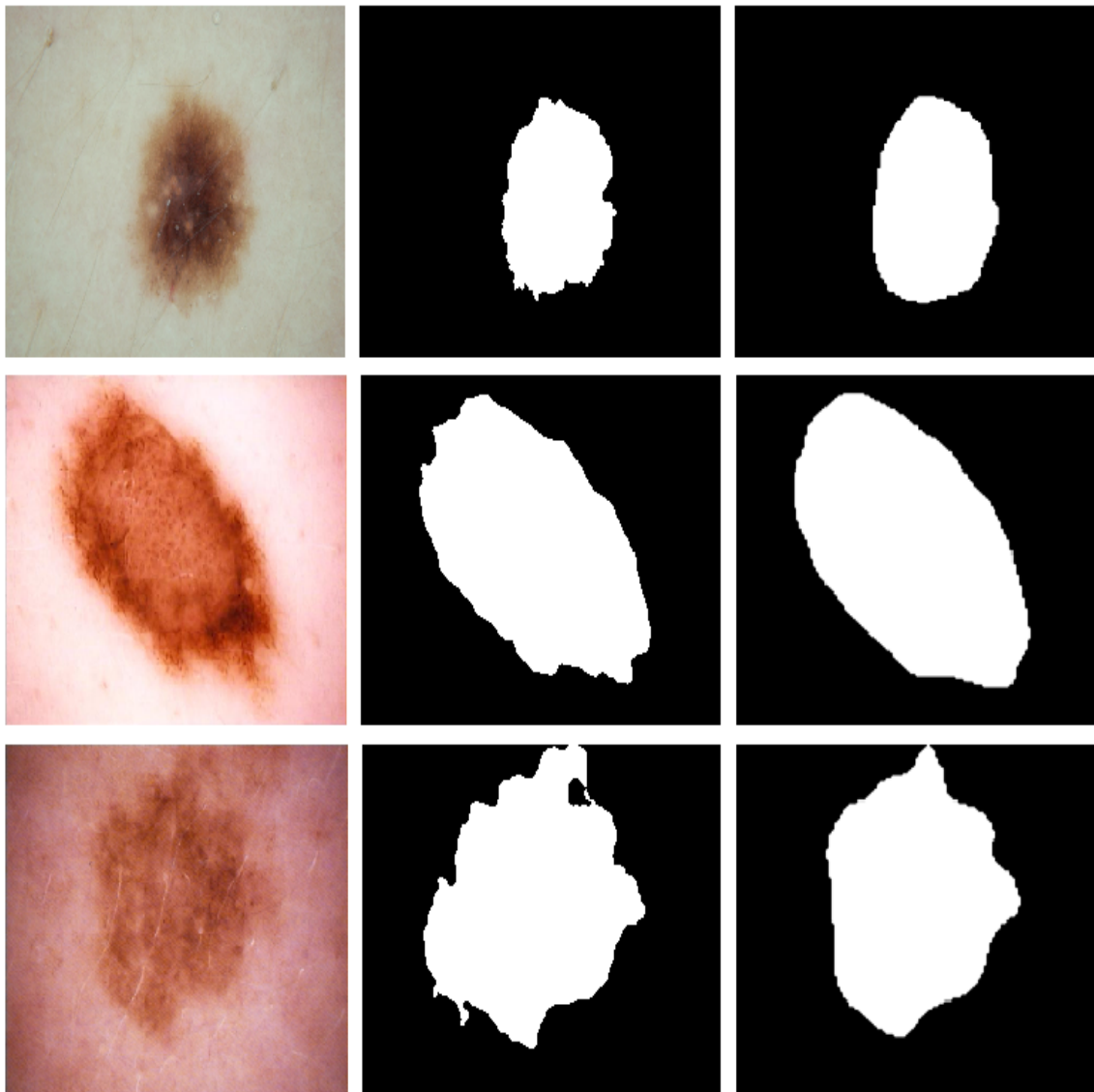


**Figure 7:** Columns from left to right correspond to: Original skin lesion images, segmentation results after the postprocessing using the RSF model with B-spline level set implementation, and the ground truth.

**Table 1**

Mean of the Jaccard index over 50 skin lesion images.

Algorithms	Jaccard (%)
RSF model with B-spline level set	86
ISIC 2018 baseline [41]	81.5

is measured by the TP, FN, and FP exactly as in [48, 49]. Table.1, demonstrates the performance of the RSF model with B-spline level set implementation, compared to the Deep learning based approach. Despite, comparison is not performed on the whole dataset ( 400 in [41] ), our algorithm yields satisfactory segmentation result with a Jaccard index equals 86%, clearly superior to the baseline one.

#### 4.4. Real image segmentation

In this section, transiently transfected *Drosophila* S2R+ cells expressing a GFP tagged protein at different levels are segmented. This section includes a figure representation of the intermediate steps of the preprocessing and the segmentation bloc, qualitative and quantitative comparison between algorithms for noiseless and noisy images.

##### 4.4.1. Representation of the preprocessing and the segmentation blocs

In this section, results of different intermediate steps (from preprocessing to segmentation bloc) for the proposed algorithm are presented for *Drosophila* 1. The preprocessing step is presented in Fig.8. It is added as mentioned in section 3 by applying the local normalization and the Gamma correction. The local normalization uniformizes the mean and the variance of the image around local neighbors.

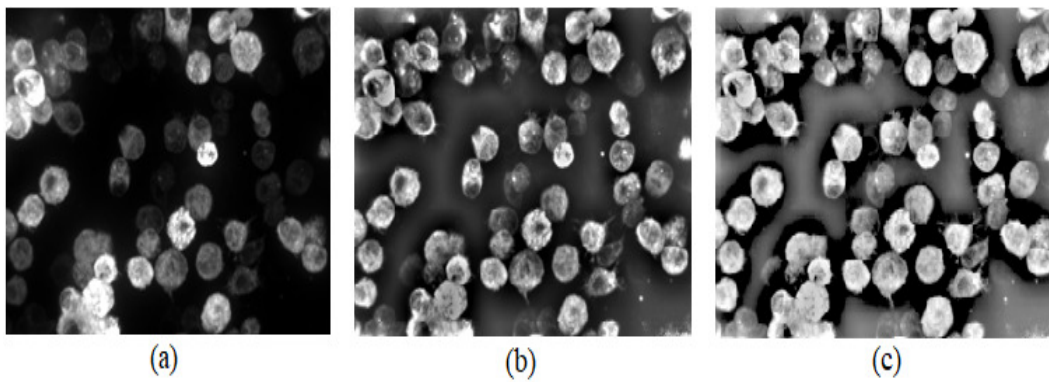


**Figure 8:** Preprocessing step: (a) Original Drosophila 1, (b) Normalized Drosophila 1, (c) Normalized Drosophila 1 with Gamma correction (Gamma= 0.4).

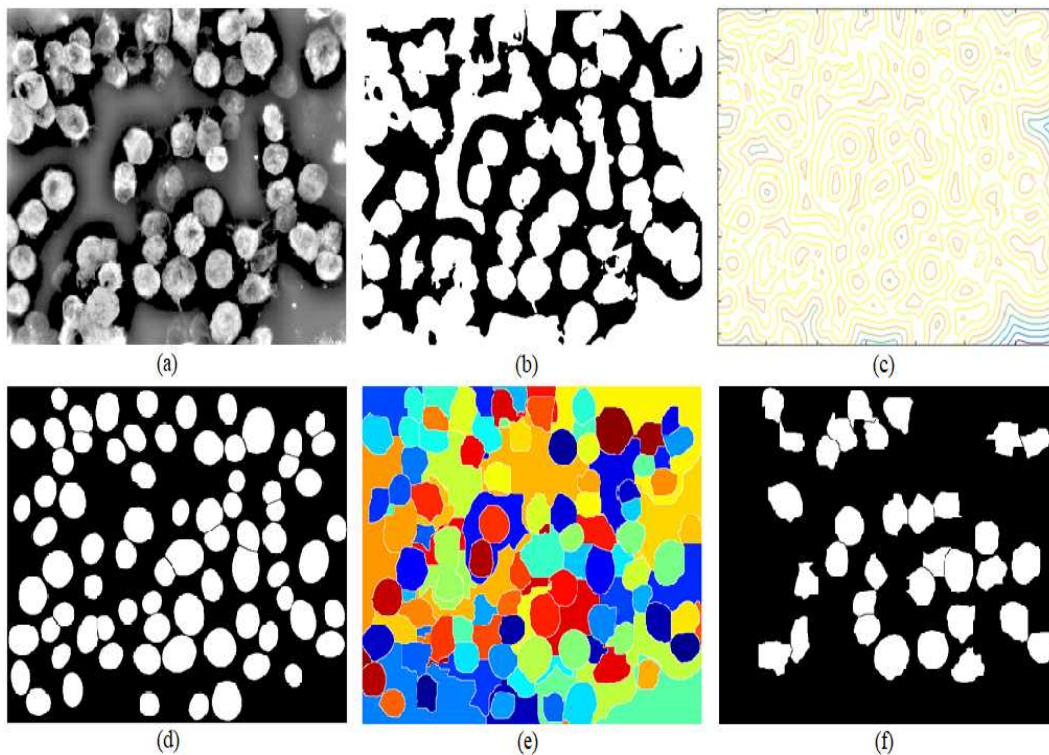


**Figure 9:** Successive steps of the segmentation bloc for Drosophila 1: (a) Preprocessed Drosophila 1, (b) Segmentation result using the RSF model with B-spline level set implementation, (c) Reverse filtered distance map of (b), (d) Image of object markers constructed using Obj.MPP, (e) Watershed result: The Watershed is applied to the reverse filtered distance map in (c), (f) Postprocessed result of Watershed for Drosophila 1.

Therefore, the darkness is reduced. On the other hand, the Gamma correction ameliorates the brightness of the image. Fig.9 illustrates the successive steps of the segmentation bloc of the B-spline-WatershedRSF algorithm applied to Drosophila 1. As shown in Fig.9-(b), applying the RSF model with B-spline level set implementation detects most of the cells. However, the refinement of contours is necessary. That proves the relevance of adding the Watershed to correctly segment the image as shown in Fig.9-(e).

#### 4.4.2. Real noiseless images Qualitative evaluation

Fig.10 presents segmentation results obtained for Drosophila 2, 3 and 4 using the B-spline-WatershedRSF. The first column (from the left) represents the preprocessed Drosophila, the presence of intensity inhomogeneity and clustered cells are noticed. Final segmentation results after the postprocessing, including only the living cells not touching image borders, are given in the second column. The third column corresponds to the ground truth of the image. The proposed

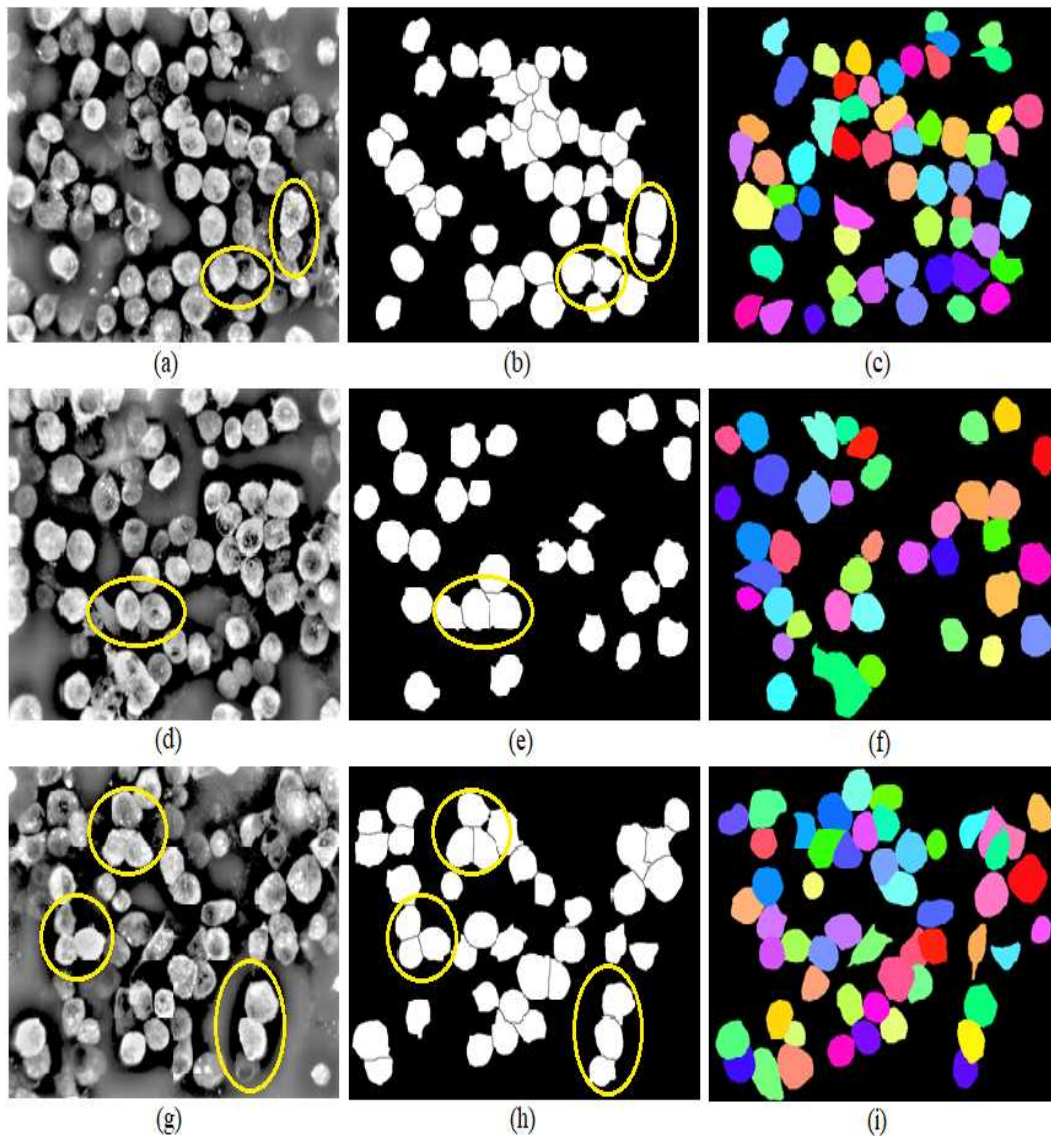


**Figure 10:** The rows 1, 2 and 3 correspond respectively to images of Drosophila 2, Drosophila 3 and Drosophila 4. The first column (from the left) corresponds preprocessed images, the second column includes final segmentation results for Drosophila 2,3 and 4, finally the third column represents the ground truth.

algorithm provides high-quality of cell segmentation. Especially, it can deal with clustered cells as shown in Fig.10-(b), (e), and (h). Different clustered cells are successfully separated as marked with yellow ellipses. In addition, the B-spline-WatershedRSF correctly detects the boundaries of Drosophila cells with different forms and sizes (even small ones). For qualitative comparison between algorithms, we present in Fig.11 segmentation results for Drosophila 2 and Drosophila 3. The difference in performance is explained by the fact that the B-spline-WatershedRSF uses the RSF model to consider intensity inhomogeneity within the image. On the other hand, the Watershed is applied to the RSF segmentation result rather than the image gradient, unlike the SegWatershed algorithm. Besides, with the B-spline-WatershedRSF, the advantage is gained by the relevant choice of markers defined by the Obj.MPP.

**Quantitative evaluation**

For the quantitative evaluation, results are first presented using the three algorithms without the postprocessing step in Table.2. Then, final segmentation results including the postprocessing are given in Table.3.

Table.2 includes: The first column refers to the image name, the second column to the applied algorithm, the number of cells in the Ground truth is given in the third column followed by the number of detected cells, the fifth column contains the  $F_1$  score, then TP, FN, and FP are presented, and the last column corresponds to the Jaccard index. Results confirm that our method performs better than the SegWatershed and the B-spline Chan-Vese algorithms even without a postprocessing step. As an example, the  $F_1$  score, over the five images, equals 73% for the B-spline-WatershedRSF, 64% for the SegWatershed and 56% for the

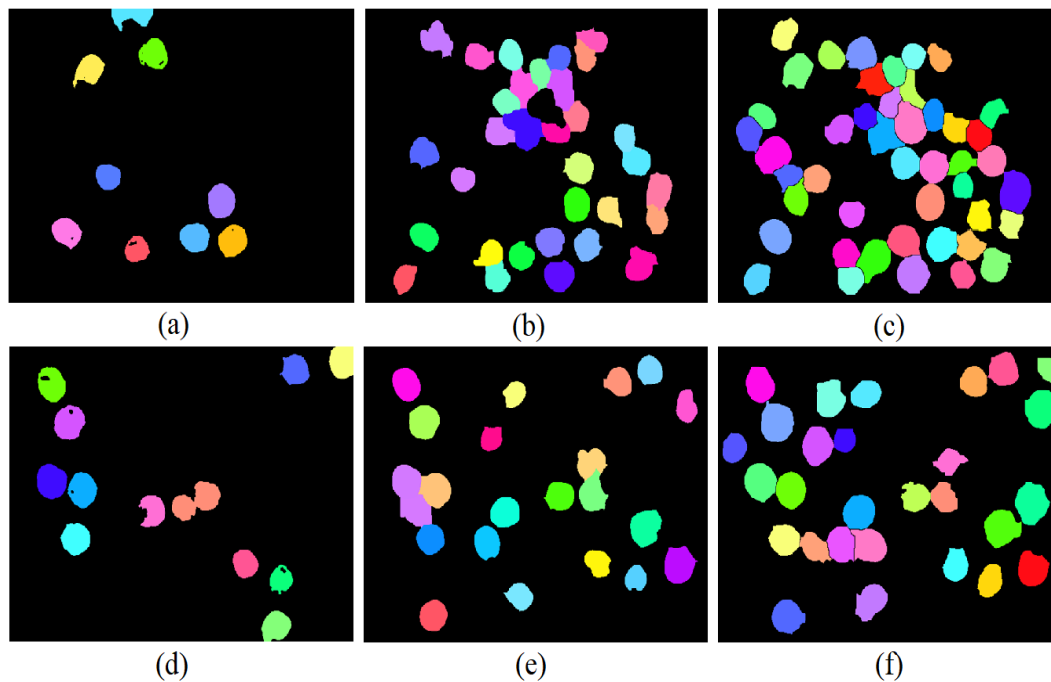


**Figure 11:** Rows 1, 2 correspond respectively to results for Drosophila 2 and Drosophila 3. The columns 1, 2 and 3 correspond respectively to: ((a)-(d)) Final segmentation result using the B-spline Chan-Vese algorithm, ((b)-(e)) Final segmentation result using the SegWatershed algorithm and ((c)-(f)) Final segmentation result using the B-spline-WatershedRSF algorithm. Use of Colors in images was necessary to distinguish the segmentation of clustered cells.

**Table 2**

Segmentation performance without postprocessing step for real images of Drosophila. The  $F_1$  score, the number of the ground truth, the number of detected cells and detection Errors measured by TP, FN, FP and the Jaccard index are compared for the B-spline-WatershedRSF, the SegWatershed and the B-spline Chan-Vese algorithms.

Images	Methods	N Ground Truth	N detection	$F_1$ (%)	TP	FP	FN	Jaccard (%)
Drosophila 1	<b>B-spline-WatershedRSF</b>		77	77	61	16	21	74
	SegWatershed	82	54	68	46	8	36	52
	B-spline Chan-Vese		97	61	55	42	27	46
Drosophila 2	<b>B-spline-WatershedRSF</b>		66	79	63	3	30	72
	SegWatershed	93	48	64	45	3	48	50
	B-spline Chan-Vese		129	66	73	56	20	46
Drosophila 3	<b>B-spline-WatershedRSF</b>		65	79	60	5	26	72
	SegWatershed	86	60	73	53	7	33	52
	B-spline Chan-Vese		74	67	54	20	32	49
Drosophila 4	<b>B-spline-WatershedRSF</b>		54	79	52	2	26	76
	SegWatershed	78	42	63	38	4	40	44
	B-spline Chan-Vese		98	58	51	47	27	41
Drosophila 5	<b>B-spline-WatershedRSF</b>		21	53	21	0	37	75
	SegWatershed	58	23	54	22	1	36	52
	B-spline Chan-Vese		241	27	41	200	17	41

B-spline Chan-Vese. Besides, the Jaccard index, over the five images, exceeds 74% for the B-spline-WatershedRSF while it is only 50% for the SegWatershed and 45% for the B-spline Chan-Vese. Table.3 illustrates the quantitative performances of the algorithms after the postprocessing step, the same metrics are used as in Table.2. For the proposed algorithm B-spline-WatershedRSF, when comparing results in Table 2 and 3 it is noted that the performance

is improved for all the images: the  $F_1$  score and Jaccard index increase when including the postprocessing step while the False positive and False negative decrease. It worth pointing here, that in the context of the study, only living cells are important, therefore, the postprocessing consists in deleting the dead cells from the final segmentation result. As expected the amount of detection and the true positive decreases with the postprocessing, this is a consequence of



**Table 3**

Segmentation performance with postprocessing step for real images of Drosophila. The  $F_1$  score, the number of the ground truth, the number of detected cells and detection Errors measured by TP, FN, FP and the Jaccard index are compared for the B-spline-WatershedRSF, the SegWatershed and the B-spline Chan-Vese algorithms.

Images	Methods	N Ground Truth	N detection	$F_1$ (%)	TP	FP	FN	Jaccard (%)
Drosophila 1	<b>B-spline-WatershedRSF</b>		33	71	27	6	16	74
	SegWatershed	43	22	65	21	1	22	69
	B-spline Chan-Vese		7	24	6	1	37	75
Drosophila 2	<b>B-spline-WatershedRSF</b>		45	87	45	0	14	73
	SegWatershed	59	32	70	32	0	27	75
	B-spline Chan-Vese		9	24	8	1	51	85
Drosophila 3	<b>B-spline-WatershedRSF</b>		28	81	27	1	12	80
	SegWatershed	39	22	72	22	0	17	85
	B-spline Chan-Vese		12	39	10	2	29	83
Drosophila 4	<b>B-spline-WatershedRSF</b>		40	83	39	1	15	79
	SegWatershed	54	30	67	28	2	26	77
	B-spline Chan-Vese		1	4	1	0	53	86
Drosophila 5	<b>B-spline-WatershedRSF</b>		13	68	13	0	12	83
	SegWatershed	25	11	61	11	0	14	76
	B-spline Chan-Vese		4	28	4	0	21	90

eliminating the dead cells. To conclude, the postprocessing step ameliorates the overall performance and respects the constraint on the final segmentation result to maintain only living cells. On the other hand, as shown by the number of detections (column 3), the B-spline-WatershedRSF detects a greater number of cells than the SegWatershed algorithm and the B-spline Chan-Vese. Regarding false detections, as illustrated in the FP column of Table.3, except for the first image, the B-spline-WatershedRSF provides the lower number of FP. The same conclusion is drawn for the  $F_1$  score: For all images, the proposed algorithm provides the highest score. The  $F_1$  score, over the five images, equals 78% for the B-spline-WatershedRSF algorithm, 67% for the SegWatershed algorithm and only 24% for the B-spline Chan-Vese. Regarding all the above-cited criteria, the B-spline-WatershedRSF performs better than the B-spline Chan-Vese and the SegWatershed in terms of cell detection. The last column is dedicated to the Jaccard index. The latter is a measure of the intersection with the ground truth, therefore calculated only when there is an intersection between the segmented image and the ground truth, i.e. for the true positive. Besides, the difference in performance between algorithms is explained by the sensitivity of the Jaccard index to the geometry of the detected cell. In fact, with the B-spline-WatershedRSF, the number of true positives is high (column of the TP). However, weak shape segmentation of few detected cells severely penalizes the Jaccard index. The opposite is true for the B-spline Chan-Vese where the number of true positives is low while the geometry of the detected cells is good, which increases the Jaccard index. The overall performance is appreciated using the  $F_1$  score for the number of detections and the Jaccard index for the quality of segmentation of the detected cells.

To compare the statistics of results for the three algorithms, we include box plot representations of the  $F_1$  score and the Jaccard index. Fig.12. Except for one case (the box at the second line and the second column) that is explained above, the rest of boxes representing the performance of the proposed algorithm are the higher ones indicating the superiority of the B-spline-WatershedRSF in terms of the  $F_1$  score and the Jaccard index and compared to the SegWatershed and the B-spline Chan-Vese algorithms. Besides, it is noted that the boxes are compacted, attesting similar performance between the different images. Regarding the proposed algorithm, the medium value, over the five images of Drosophila, is high for the  $F_1$  score and the Jaccard index.

#### 4.4.3. Real noisy images

##### Qualitative evaluation

To assess the robustness of the B-spline-WatershedRSF in the presence of noise, we performed the segmentation of real biological images with additive Gaussian noise. Fig.13 presents results of segmentation for Drosophila 4 using the B-spline-WatershedRSF. Fig.13-(a) and (c) present respectively the noiseless preprocessed Drosophila 4 and the noisy one with SNR= 15dB, Fig.13-(b) and (d) correspond respectively to the final segmentation result for the noiseless preprocessed Drosophila 4 and for the noisy one. When observing Fig.13-(b) and (d), it is clear that the noise does not significantly impact the segmentation performance: Most of the cells are well detected as in the noiseless images.

##### Quantitative evaluation

To numerically illustrate the robustness of the proposed algorithm to the noise, the Jaccard index, the  $F_1$  score and the variance of the  $F_1$  score are calculated for high and medium SNR: 15dB and 30dB. They are obtained by averaging 10 segmentation results through different noise realizations. As shown in Table.4 for SNR=15dB, the  $F_1$  score, over the

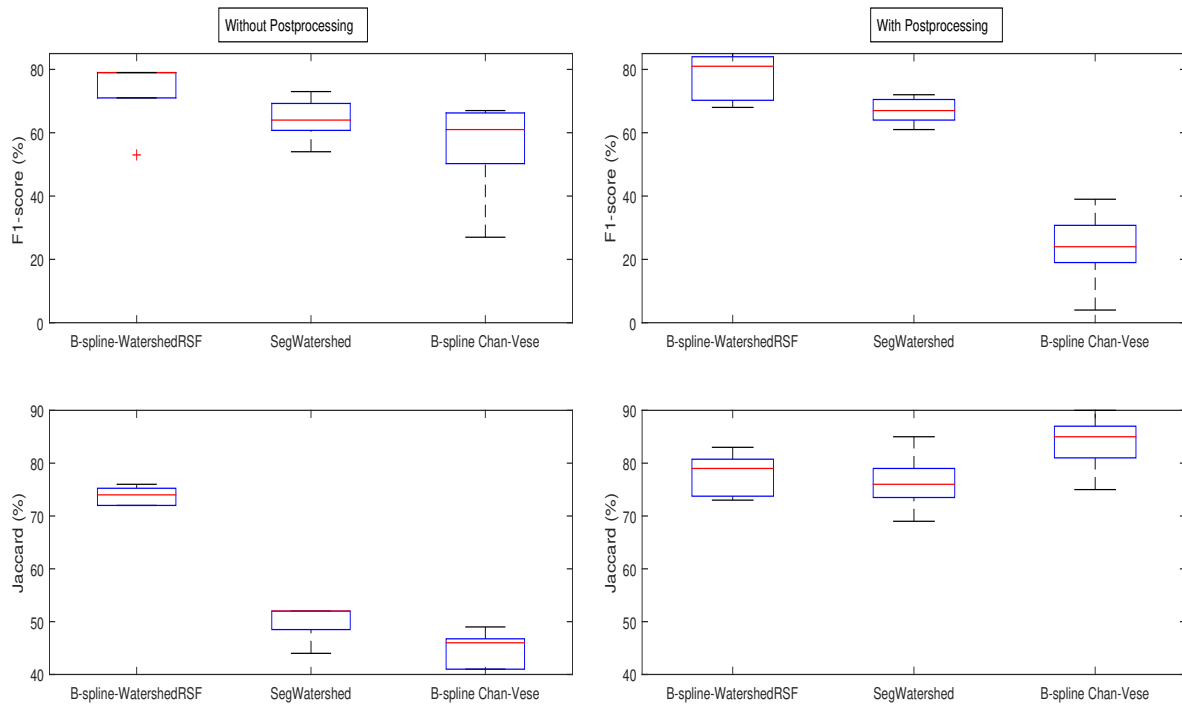


**Figure 12:** Quantitative comparison of B-spline-WatershedRSF with SegWatershed and B-spline Chan-Vese applied to noiseless *Drosophila* images. The first and second columns include respectively results without and with postprocessing.

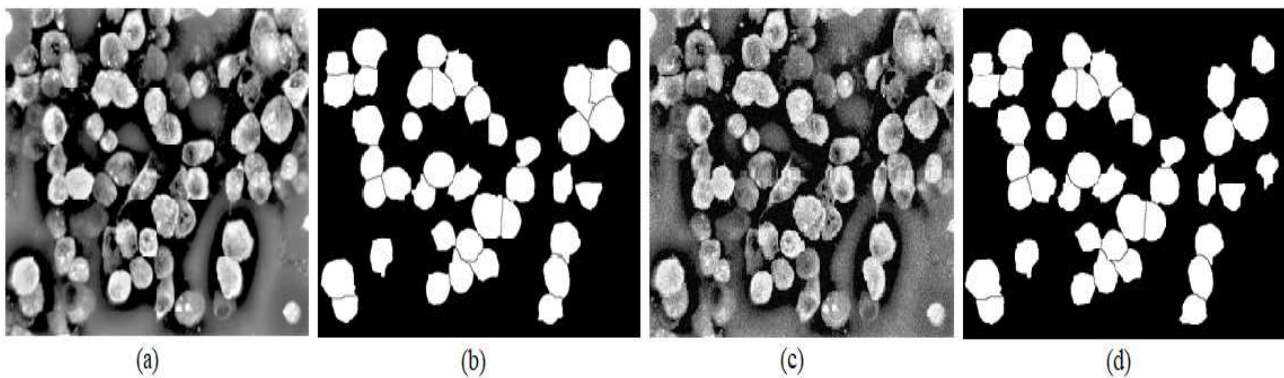


**Figure 13:** (a) Preprocessed *Drosophila* 4 without additive Gaussian noise, (b) Final segmentation result for (a), (c) Preprocessed *Drosophila* 4 with additive Gaussian noise  $SNR=15dB$ , (d) Final segmentation result for (c).

**Table 4**

$F_1$  score, variance of  $F_1$  score and Jaccard index for real images of *Drosophila*. Results with postprocessing step are obtained by averaging 10 realizations on every noise level  $SNR = 30dB$  and  $SNR = 15dB$ .

Images	SNR	$F_1$ (%)	$F_1$ variance	Jaccard (%)
Drosophila 1	30dB	71	$2.538710^{-05}$	74
	15dB	68	$1.318010^{-04}$	76
Drosophila 2	30dB	86	$3.238410^{-05}$	75
	15dB	86	$1.656710^{-04}$	74
Drosophila 3	30dB	80	$5.824210^{-05}$	81
	15dB	79	$2.391010^{-04}$	80
Drosophila 4	30dB	83	$7.696610^{-05}$	79
	15dB	83	$3.692610^{-05}$	80
Drosophila 5	30dB	68	$4.889810^{-04}$	85
	15dB	68	$3.920210^{-04}$	85

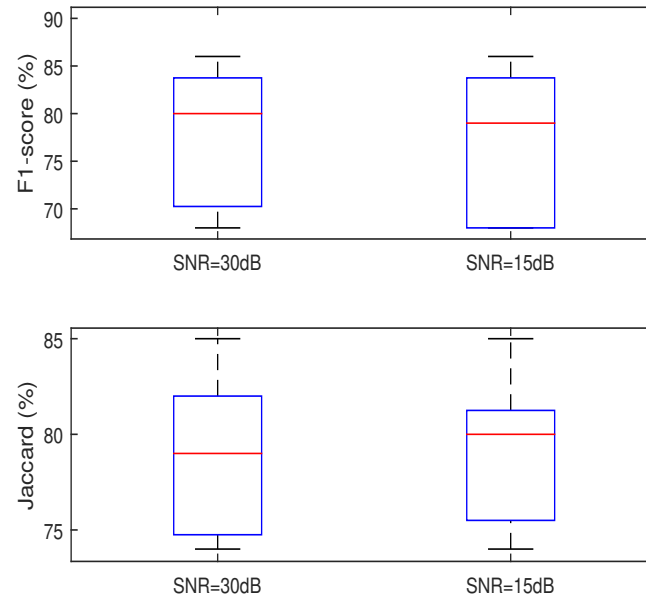


**Figure 14:** Quantitative evaluation of B-spline-WatershedRSF applied to noisy Drosophila images.

five images, is greater than 76% with reduced variance, the latter attests that the  $F_1$  score is centered around the mean value for different realizations. On the other hand, good performances are maintained compared to the results obtained for noiseless images: The  $F_1$  score equals 79% for Drosophila 3 (SNR=15dB), and it equals 81% for the same noiseless image. Even more, for the Drosophila 4, the  $F_1$  score equals 83% for noiseless case and remains the same with different noise levels (15dB and 30dB). Besides, the quality of segmentation is not degrading with the presence of noise. These conclusions are confirmed by the Jaccard index. For the five considered images, the Jaccard index is greater than or equal to 74%. Results confirm that the B-spline-WatershedRSF is robust to different levels of noise. A different representation of the quantitative evaluation is given in Fig.14 by the boxes of the  $F_1$  score and the Jaccard index. Mediums values are not changing significantly which confirm the robustness of the B-spline-WatershedRSF to different levels of noise.

#### 4.5. Simulated image segmentation

In this section, the B-spline-WatershedRSF algorithm is applied to a set of simulated images, generated using the Simcep simulator [44]. Different levels of noise and luminance are considered to reproduce biological image defects and mimic the real image appearance. Since the images are simulated, neither preprocessing nor postprocessing are needed and only the segmentation bloc of the B-spline-WatershedRSF algorithm is applied (see Fig.2). Due to the limited space for images without clustered cells, quantitative evaluation is only presented, while for images with clustered cells qualitative one is shown.

##### 4.5.1. Images without clustered cells

As shown in Table.5, the number of detected cells for the B-spline-WatershedRSF is high compared to SegWatershed and B-spline Chan-Vese algorithms. Same observations are given in Fig.15. High Medium values of the Jaccard index and the  $F_1$  score are noted for the B-spline-WatershedRSF, compared to the SegWatershed and the B-spline Chan-Vese algorithms, which indicates that the proposed algorithm match better with corresponding ground truth. Besides, the boxes are compacted which indicates the good performance of the proposed algorithm in segmenting all simcep images.

Using the  $F_1$  score (over the four images), the B-spline-WatershedRSF ( $F_1=88\%$ ) outperforms the other algorithms (76% for SegWatershed algorithm, 26% for the B-spline Chan-Vese algorithm). Besides, as indicated in the FP column, the B-spline Chan-Vese generates a large number of false positives since it is sensitive to noise distortion and it fails to deal with the presence of high luminance and intensity inhomogeneity. Again, this point out the relevance of the B-spline-WatershedRSF in managing the noise and the intensity inhomogeneity. Besides, the B-spline-WatershedRSF provides a high Jaccard index. Over the four images, it equals 90% which attests the quality of cell segmentation. Furthermore, to point out the effectiveness of our algorithm, statistics are calculated on larger dataset including 50 Simcep images. In Table.6, the mean of the  $F_1$  score and the Jaccard index are calculated for the B-spline-WatershedRSF, the SegWatershed, and the B-spline Chan-Vese. As illustrated in Table.6, even for larger dataset, the B-spline-WatershedRSF provides a high segmentation performance with Jaccard index and  $F_1$  score exceed 80%.

**Table 5**

Segmentation performance for simulated images. The  $F_1$  score, the number of the ground truth, the number of detected cells and detection Errors measured by TP, FN, FP and the Jaccard index are compared for the B-spline-WatershedRSF, the SegWatershed and the B-spline Chan-Vese algorithms.

Images	Methods	N Ground Truth	N detection	$F_1$ (%)	TP	FP	FN	Jaccard (%)
Simcep 1	<b>B-spline-WatershedRSF</b>		26	93	26	0	4	88
	SegWatershed	30	18	75	18	0	12	97
	B-spline Chan-Vese		217	23	28	189	2	86
Simcep 2	<b>B-spline-WatershedRSF</b>		21	82	21	0	9	88
	SegWatershed	30	18	75	18	0	12	93
	B-spline Chan-Vese		53	43	18	35	12	79
Simcep 3	<b>B-spline-WatershedRSF</b>		23	87	23	0	7	93
	SegWatershed	30	18	75	18	0	12	95
	B-spline Chan-Vese		255	19	27	228	3	83
Simcep 4	<b>B-spline-WatershedRSF</b>		24	89	24	0	6	92
	SegWatershed	30	19	78	19	0	11	95
	B-spline Chan-Vese		151	21	19	132	11	81

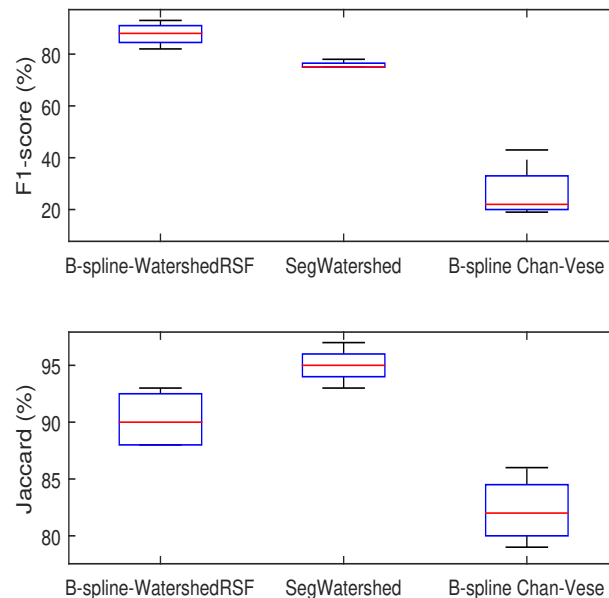


**Figure 15:** Quantitative comparison of B-spline-WatershedRSF with SegWatershed and B-spline Chan-Vese applied to Simcep images.

#### 4.5.2. Images with clustered cells

In the following, the proposed algorithm is evaluated using Simcep 5 and 6 containing clusters and overlapping cells, Fig.16. This is a challenge in image segmentation due to the difficulty in separating aggregated cells. In Fig.16-(a)-(c), difficulties related to cell clustering and intensity variations are clearly noticeable (at least five blocks of clustered cells). Segmentation results are presented in Fig.16-(b)-(d) for Simcep 5 and Simcep 6 respectively. As observed, the B-spline-WatershedRSF correctly segments the image and accurately separates a number of grouped cells.

#### 4.6. Convergence criterion and computation time

##### Convergence criterion

The algorithm is stopped when a threshold is reached for the difference between two successive values of the energy functional, or when a maximum number of iterations is attended (fixed to 100). Recall that the process is based on the minimization of the energy function to get the contour. To proof the convergence, we present the energy curves as a function of the number of iterations. The energy convergence is evaluated on all above-mentioned images and six representative images are shown in Fig.17. The images are representative in the sense that they include real noiseless,

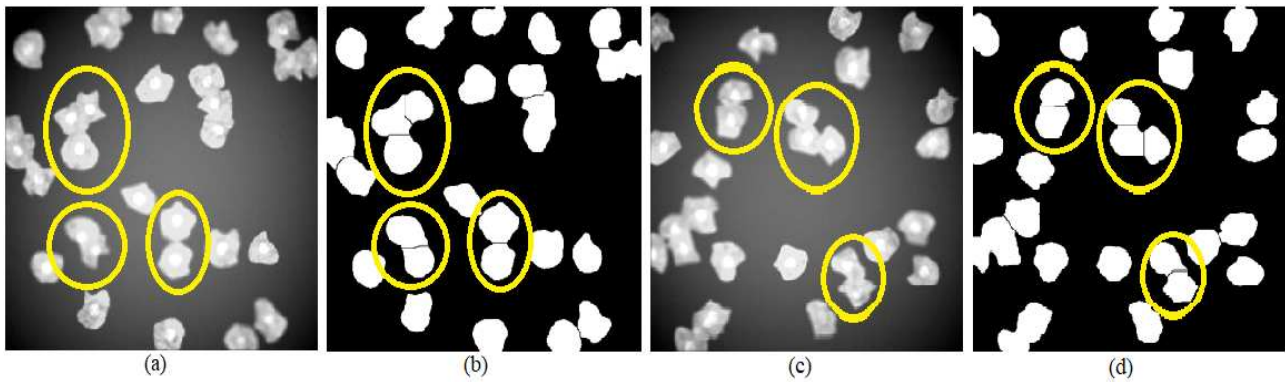


**Figure 16:** (a) Simcep 5, (b) Segmentation result for Simcep 5, (c) Simcep 6, (d) Segmentation result for Simcep 6. Clustered cells are marked with yellow ellipses. They are correctly separated by the B-spline-WatershedRSF.

**Table 6**

Segmentation performance over 50 Simcep images. The  $F_1$  score and the Jaccard index are compared for the B-spline-WatershedRSF, the SegWatershed and the B-spline Chan-Vese.

	B-spline WatershedRSF	B-spline Chan-Vese	SegWatershed
$F_1$ score (%)	94	80	73
Jaccard (%)	81	84	68

**Table 7**

Computation time in minute for different categories of images segmented using the B-spline-WatershedRSF.

Real noiseless images	Real noisy images	Simulated images	Synthetic images
20.04	20.93	13.80	0.10

real noisy and simulated data images. It can be seen from Fig.17 that the proposed algorithm converge. Satisfactory results can be generally obtained in less than 40 iterations, even in the presence of the noise.

#### Computation time

We present in Table.7 the computation time of the algorithm. This includes the postprocessing step only for the real images and the principal segmentation bloc for all. However, it is worth noting that the Watershed step is performed instantly and do not really increase the overall time. The experiments are carried out on 1.5-GHz Intel Core i5 with 16 GB of RAM. Note that the computation time is calculated for all the experiments and the mean time in minute is given in Table.7. For example, the first column indicates the mean of the time cost over the five considered noiseless images of Drosophila. As expected, the algorithm is faster for simulated images than for real ones. However, for the latter only a bit increase is noted when including noise. Finally, it is important to note the difficulties inherent the considered biological images that explain the required time for calculation. The synthetic images, Fig.3 include

fewer contents. Therefore, only few second are sufficient to perform the segmentation.

## 5. Conclusion

In this paper, we propose a new method for biological image segmentation based on the B-spline formulation. After applying the RSF model with B-spline level set implementation, the contours of detected cells are refined using the Watershed algorithm. The use of the RSF model allows consideration of the intensity inhomogeneity within the image, while the relevant choice of markers in the Watershed improves the quality of segmentation with the separation of clustered cells. Results encompass a special focus on real images containing transiently transfected Drosophila S2R+ cells. In addition, skin lesion images and simulated images are considered. Qualitative and quantitative evaluations are attested through many experiments and comparisons with existing methods. They both demonstrate the high quality of cell segmentation using the B-spline-WatershedRSF. Most importantly, the proposed method successfully manages the intensity inhomogeneity and clustered cells within biological images. Besides, it is resistant to different levels of noise. From a methodological standpoint, several perspectives can be considered: 1) To develop an efficient way to tune the hyperparameters of the algorithm, for example by learning the best values of these hyperparameters using the deep Learning approach, 2) To introduce an interpolation method for partially segmented cells, to detect the missing part of a cell's contour. From the applicative perspective, we plan to take further advantage of the performance of the B-spline-WatershedRSF in other clinical datasets or biomedical fields (e.g., proteomics, transcriptomics...).

## Ethical approval

Not required, as no human or animal subjects were involved.

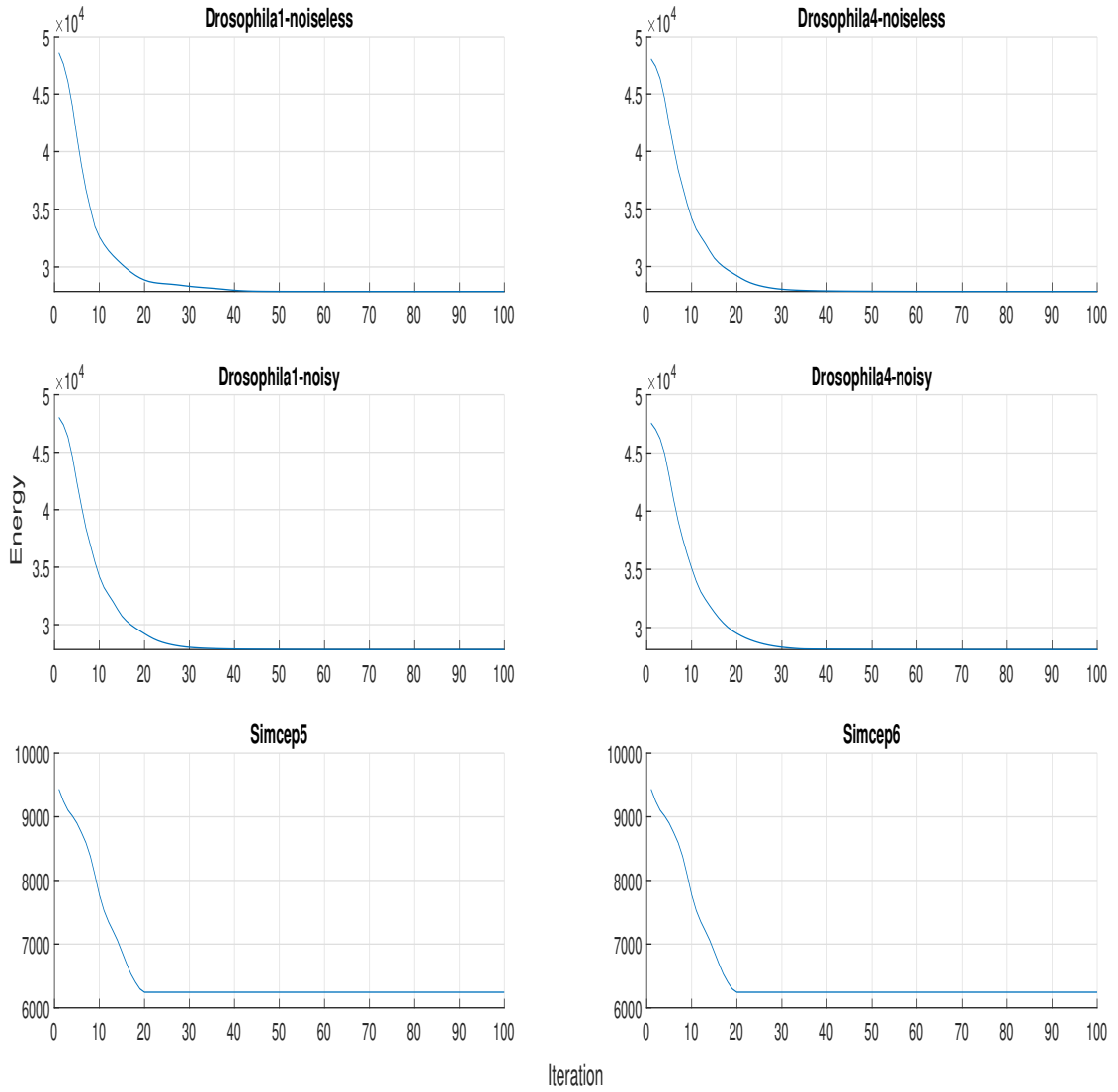


**Figure 17:** Energy curves as a function of the number of iterations for different selected images.

## Funding

This research did not receive any specific grant from funding agencies in the public, commercial, or not-for-profit sectors.

## Declaration of Competing Interest

The authors declare that they have no known competing financial interests or personal relationships that could have appeared to influence the work reported in this paper.

## Appendix A. Energy functional calculation

The energy functional  $J$  includes three terms :

$$J = J_{in} + J_{out} + J_c \quad (21)$$

with,

$$\begin{cases} J_{in} = v_{in} \int_{\Omega} \left[ \int_{\Omega} K_{\sigma}(x-y) |I(y) - f_{in}(x)|^2 H_{\epsilon}(\phi(y)) dx \right] dy \\ J_{out} = v_{out} \int_{\Omega} \left[ \int_{\Omega} K_{\sigma}(x-y) |I(y) - f_{out}(x)|^2 (1 - H_{\epsilon}(\phi(y))) dx \right] dy \\ J_c = v_c \int_{\Omega} \delta_{\epsilon}(\phi(y)) |\nabla \phi(y)| dy \end{cases}$$

Considering  $J_{in}$ , the term inside the integral is equal to :

$$\begin{aligned} & K_{\sigma}(x-y)|I(y)-f_{in}(x)|^2 H_{\varepsilon}(\phi(y)) \\ & = K_{\sigma}(x-y)[I^2(y)-2I(y)f_{in}(x)+f_{in}^2(x)] H_{\varepsilon}(\phi(y)) \end{aligned} \quad (22)$$

then, with the integration of Eq.22 with respect to x, and the introduction of the convolution product we obtain :

$$J_{in} = v_{in} \int_{\Omega} [I(y)^2 - 2I(y)(K_{\sigma} \otimes f_{in}) + (K_{\sigma} \otimes f_{in}^2)] \times H_{\varepsilon}(\phi(y)) dy \quad (23)$$

In the same manner, the following form of  $J_{out}$  is obtained as :

$$J_{out} = v_{out} \int_{\Omega} [I(y)^2 - 2I(y)(K_{\sigma} \otimes f_{out}) + (K_{\sigma} \otimes f_{out}^2)] \times (1 - H_{\varepsilon}(\phi(y))) dy \quad (24)$$

## Appendix B. Energy functional derivation

Deriving Eq.21 with regard to B-spline coefficients  $c[k]$ , we obtain :

$$\frac{\partial J}{\partial c[k]} = \frac{\partial J_{in}}{\partial c[k]} + \frac{\partial J_{out}}{\partial c[k]} + \frac{\partial J_c}{\partial c[k]} \quad (25)$$

with,

$$\begin{aligned} \frac{\partial J_{out}}{\partial c[k]} & = \frac{\partial J_{out}}{\partial \phi(y)} \times \frac{\partial \phi(y)}{\partial c[k]} = \frac{\partial J_{out}}{\partial \phi(y)} \times \beta^n \left( \frac{y}{h} - k \right) \\ \frac{\partial J_{in}}{\partial c[k]} & = \frac{\partial J_{in}}{\partial \phi(y)} \times \frac{\partial \phi(y)}{\partial c[k]} = \frac{\partial J_{in}}{\partial \phi(y)} \times \beta^n \left( \frac{y}{h} - k \right) \\ \frac{\partial J_c}{\partial c[k]} & = \frac{\partial J_c}{\partial \phi(y)} \times \frac{\partial \phi(y)}{\partial c[k]} = \frac{\partial J_c}{\partial \phi(y)} \times \beta^n \left( \frac{y}{h} - k \right) \end{aligned} \quad (26)$$

since,

$$\frac{\partial \phi(y)}{\partial c[k]} = \beta^n \left( \frac{y}{h} - k \right) \quad (27)$$

and,

$$\frac{\partial J_{in}}{\partial c[k]} = v_{in} \int_{\Omega} \int_{\Omega} \left[ \frac{\partial F_{in}(x,y)}{\partial \phi(y)} H_{\varepsilon}(\phi(y)) + \frac{\partial H_{\varepsilon}(\phi(y))}{\partial \phi(y)} F_{in}(x,y) \right] \times \beta^n \left( \frac{y}{h} - k \right) dx dy \quad (28)$$

with,

$$F_{in}(x,y) = K_{\sigma}(x-y)|I(y)-f_{in}|^2$$

given that  $F_{in}(x,y)$  is independent of  $\phi(y)$  then,  $\frac{\partial F_{in}(x,y)}{\partial \phi(y)} =$

0, and  $\frac{\partial H_{\varepsilon}(\phi(y))}{\partial \phi(y)} = \delta_{\varepsilon}(\phi(y))$ , Eq.28 leads to :

$$\frac{\partial J_{in}}{\partial c[k]} = v_{in} \int_{\Omega} \int_{\Omega} F_{in}(x,y) \delta_{\varepsilon}(\phi(y)) \beta^n \left( \frac{y}{h} - k \right) dx dy \quad (29)$$

Same thing for  $J_{out}$  to obtain :

$$\frac{\partial J_{out}}{\partial c[k]} = -v_{out} \int_{\Omega} \int_{\Omega} F_{out}(x,y) \delta_{\varepsilon}(\phi(y)) \beta^n \left( \frac{y}{h} - k \right) dx dy \quad (30)$$

with,

$$F_{out} = K_{\sigma}(x-y)|I(y)-f_{out}|^2$$

Using Eqs.25, 29 and 30, besides separating the term on x and y in the gradient of the energy function, we obtain :

$$\begin{aligned} \frac{\partial J}{\partial c[k]} & = \int_{\Omega} \left[ \tilde{w}(y) \beta^n \left( \frac{y}{h} - k \right) \right] dy \\ & - \int_{\Omega} w_c(y) \beta^n \left( \frac{y}{h} - k \right) dy \end{aligned} \quad (31)$$

with,

$$\begin{aligned} \tilde{w}(y) & = v_{in} \int_{\Omega} F_{in}(x,y) \delta_{\varepsilon}(\phi(y)) dx \\ & - v_{out} \int_{\Omega} F_{out}(x,y) \delta_{\varepsilon}(\phi(y)) dx \end{aligned} \quad (32)$$

which is also equivalent to:

$$\begin{aligned} \tilde{w}(y) & = \int_{\Omega} K_{\sigma}(x-y) v_{in} |I(y)-f_{in}(x)|^2 \delta_{\varepsilon}(\phi(y)) dx \\ & - \int_{\Omega} K_{\sigma}(x-y) v_{out} |I(y)-f_{out}(x)|^2 \delta_{\varepsilon}(\phi(y)) dx \end{aligned} \quad (33)$$

and

$$w_c(y) = v_c \operatorname{div} \left( \frac{\nabla \phi(y)}{\|\nabla \phi(y)\|} \right) \delta_{\varepsilon}(\phi(y)) \quad (34)$$

by developing the remarkable identity in Eq.33, we obtain:

$$\tilde{w} = \tilde{w}_1 + \tilde{w}_2 + \tilde{w}_3 \quad (35)$$

with,

$$\begin{aligned} \tilde{w}_1 & = I^2(y)(v_{in} - v_{out}) \left( \int_{\Omega} K_{\sigma}(x-y) dx \right) \delta_{\varepsilon}(\phi(y)) \\ & = I^2(y)(v_{in} - v_{out}) \delta_{\varepsilon}(\phi(y)) \end{aligned} \quad (36)$$

$$\begin{aligned} \tilde{w}_2 & = 2I(y) \left( \int_{\Omega} (v_{out} f_{out}(x) - v_{in} f_{in}(x)) K_{\sigma}(x-y) dx \right) \delta_{\varepsilon}(\phi(y)) \\ & = 2I(y) [K_{\sigma} \otimes (v_{out} f_{out}(x) - v_{in} f_{in}(x))] \delta_{\varepsilon}(\phi(y)) \end{aligned} \quad (37)$$

$$\begin{aligned} \tilde{w}_3 & = \left( \int_{\Omega} (v_{in} f_{in}^2(x) - v_{out} f_{out}^2(x)) K_{\sigma}(x-y) dx \right) \delta_{\varepsilon}(\phi(y)) \\ & = [K_{\sigma} \otimes (v_{in} f_{in}^2 - v_{out} f_{out}^2)] \delta_{\varepsilon}(\phi(y)) \end{aligned} \quad (38)$$

## References

- [1] H. Liu, S. Liu, D. Guo, Y. Zheng, P. Tang, G. Dan, Original intensity preserved inhomogeneity correction and segmentation for liver magnetic resonance imaging, *Biomedical Signal Processing and Control* 47 (2019) 231–239.
- [2] G. Xiao, M. Brady, J. A. Noble, Y. Zhang, Segmentation of ultrasound b-mode images with intensity inhomogeneity correction, *IEEE Transactions on medical imaging* 21 (2002) 48–57.
- [3] G. Xiong, X. Zhou, L. Ji, P. Bradley, N. Perrimon, S. Wong, Segmentation of drosophila mri fluorescence images using level sets, *Int Conference on Image Processing ICIP* (2006) 73–76.
- [4] P. Yan, X. Zhou, M. Shah, S. T. C. Wong, Automatic segmentation of high-throughput mri fluorescent cellular images, *IEEE Trans on Information Technology in Biomedicine* 12 (2008) 109–117.
- [5] T. R. Jones, A. Carpenter, P. Golland, Voronoi-based segmentation of cells on image manifolds, *Workshop Comput. Vis. Biomed. Image Appl. (CVBIA)* (2005) 535–543.
- [6] X. Zhou, K. Liu, P. Bradley, N. Perrimon, S. Wong, Towards automated cellular image segmentation for mri genome-wide screening, *Medical image computing and computer-assisted intervention: MICCAI. International Conference on Medical Image Computing and Computer-Assisted Intervention* 8 (2005) 885–892.
- [7] N. Otsu, A threshold selection method from gray-level histograms, *IEEE transactions on systems, man, and cybernetics* 9 (1979) 62–66.
- [8] R. Rahali, Y. Ben Salem, N. Dridi, H. Dahman, Drosophila image segmentation using marker controlled watershed, *17th International Multi-Conference on Systems, Signals and Devices SSD* (2020) 191–195.
- [9] M. Kass, A. Witkin, D. Terzopoulos, Snakes: Active contour models, *International journal of computer vision* 1 (1988) 321–331.
- [10] V. Caselles, R. Kimmel, G. Sapiro, Geodesic active contours, *International journal of computer vision* 22 (1997) 61–79.
- [11] R. Ronfard, Region-based strategies for active contour models, *International journal of computer vision* 13 (1994) 229–251.
- [12] T. F. Chan, L. A. Vese, Active contours without edges, *IEEE Transactions on image processing* 10 (2001) 266–277.
- [13] P. Getreuer, Chan-vese segmentation, *Image Processing On Line* 2 (2012) 214–224.
- [14] X. Du, W. Pan, T. D. Bui, Text line segmentation in handwritten documents using mumford–shah model, *Pattern Recognition* 42 (2009) 3136–3145.
- [15] C. Li, C. Kao, J. C. Gore, Z. Ding, Minimization of region-scalable fitting energy for image segmentation, *IEEE transactions on image processing: a publication of the IEEE Signal Processing Society* 17 (2008) 1940.
- [16] C. He, Y. Wang, Q. Chen, Active contours driven by weighted region-scalable fitting energy based on local entropy, *Signal Processing* 92 (2012) 587–600.
- [17] C. Feng, J. Yang, C. Lou, W. Li, K. Yu, D. Zhao, A global inhomogeneous intensity clustering- (ginc-) based active contour model for image segmentation and bias correction, *Computational and Mathematical Methods in Medicine* 2020 (2020) 1–18.
- [18] O. Bernard, D. Friboulet, P. Thévenaz, M. Unser, Variational b-spline level-set: a linear filtering approach for fast deformable model evolution, *IEEE Transactions on Image Processing* 18 (2009) 1179–1191.
- [19] R. Rahali, Y. Ben Salem, N. Dridi, H. Dahman, B-spline level set for drosophila image segmentation, *IEEE International conference on Image Processing ICIP* (2020) 413–417.
- [20] X. Yang, H. Li, X. Zhou, Nuclei segmentation using marker-controlled watershed, tracking using mean-shift, and kalman filter in time-lapse microscopy, *IEEE Transactions on Circuits and Systems I: Regular Papers* 53 (2006) 2405–2414.
- [21] M. A. Khan, I. U. Lali, A. Rehman, M. Ishaq, M. Sharif, T. Saba, S. Zahoor, T. Akram, Brain tumor detection and classification: A framework of marker-based watershed algorithm and multilevel priority features selection, *Microscopy research and technique* 82 (2019) 909–922.
- [22] F. De Graeve, E. Debreuve, S. Rahmoun, S. Ecsedi, A. Bahri, A. Hubstenberger, X. Descombes, F. Besse, Detecting and quantifying stress granules in tissues of multicellular organisms with the obj. mpp analysis tool, *Traffic* 20 (2019) 697–711.
- [23] G. Aubert, M. Barlaud, O. Faugeras, S. Jehan-Besson, Image segmentation using active contours: Calculus of variations or shape gradients, *SIAM Journal on Applied Mathematics* 63 (2003) 2128–2154.
- [24] C. Li, C. Kao, J. C. Gore, Z. Ding, Implicit active contours driven by local binary fitting energy, *2007 IEEE Conference on Computer Vision and Pattern Recognition* (2007) 1–7.
- [25] R. Tsai, S. Osher, Level set methods and their applications in image science, *Communications in mathematical sciences* 1 (2003).
- [26] S. Osher, R. Fedkiw, K. Piechor, Level set methods and dynamic implicit surfaces, *Appl. Mech. Rev.* 57 (2004) B15.
- [27] J. S. Suri, K. Liu, S. Singh, S. N. Laxminarayan, X. Zeng, L. Reden, Shape recovery algorithms using level sets in 2-d/3-d medical imagery: a state-of-the-art review, *IEEE Transactions on information technology in biomedicine* 6 (2002) 8–28.
- [28] C. Li, R. Huang, Z. Ding, J. C. Gatenby, D. N. Metaxas, J. C. Gore, A level set method for image segmentation in the presence of intensity inhomogeneities with application to mri, *IEEE transactions on image processing* 20 (2011) 2007–2016.
- [29] M. Unser, Splines: a perfect fit for signal and image processing, *IEEE Signal Processing Magazine* 16 (1999) 22–38.
- [30] I. Schoenberg, Contribution to the problem of approximation of equidistant data by analytic functions, *Quart. Appl. Math* 4 (1946) 45–99, 112–141.
- [31] Pawar, A., B-spline based image segmentation, registration and modeling neuron growth., *Thesis of Carnegie Mellon University* (2020).
- [32] S. Beucher, Segmentation d'images et morphologie mathématique, *Ph. D Thesis, School of Mines* (1990).
- [33] P. T. Jackway, Gradient watershed in morphological scale-space, *IEEE Transactions on Image Processing* 5 (1996) 913–921.
- [34] S. Beucher, J. Serra, P. Soille, Watershed, hierarchical segmentation and waterfall algorithm. *mathematical morphology and its applications to image processing*, Springer (1994) 69–76.
- [35] X. Descombes, Multiple objects detection in biological images using a marked point process framework, *Methods* 115 (2017) 2–8.
- [36] A. Gamal-Eldin, X. Descombes, G. Charpiat, J. Zerubia, A fast multiple birth and cut algorithm using belief propagation, *2011 18th IEEE International Conference on Image Processing* (2011) 2813–2816.
- [37] N. Brady, D. J. Field, Local contrast in natural images: normalisation and coding efficiency, *Perception* 29 (2000) 1041–1055.
- [38] S. Rahman, M. M. Rahman, M. Abdullah-Al-Wadud, G. D. Al-Quaderi, M. Shoyab, An adaptive gamma correction for image enhancement, *EURASIP Journal on Image and Video Processing* (2016) 1–13.
- [39] B. Li, S. Acton, Active contour external force using vector field convolution for image segmentation, *IEEE Transactions on Image Processing* 16 (2007) 2096–2106.
- [40] B. Li, Parametric toolbox, <https://www.mathworks.com/matlabcentral/fileexchange/22871-parametricactive-model-toolbox> (2020).
- [41] Q. Yuan, Isic 2018: Skin lesion analysis towards melanoma detection., <https://github.com/yuanqing811/ISIC2018> (2018).
- [42] C. Goutte, E. Gaussier, A probabilistic interpretation of precision, recall and f-score, with implication for evaluation, *Lecture notes in computer science* (2005) 345–359.
- [43] R. Shi, K. N. Ngan, S. Li, Jaccard index compensation for object segmentation evaluation, *2014 IEEE international conference on image processing (ICIP)* (2014) 4457–4461.
- [44] A. Lehmußola, P. Ruusuvuori, J. Selinummi, H. Huttunen, O. Yli-Harja, Computational framework for simulating fluorescence microscope images with cell populations, *IEEE transactions on medical imaging* 26 (2007) 1010–1016.



- [45] M. Huang, W. Yu, D. Zhu, An improved image segmentation algorithm based on the otsu method, 13th ACIS International Conference on Software Engineering, Artificial Intelligence, Networking and Parallel/Distributed Computing (2012) 135–139.
- [46] Y. Li, B. Sixou, F. Peyrin, A review of the deep learning methods for medical images super resolution problems, IRBM 42 (2021) 120–133.
- [47] R. El Jurdi, C. Petitjean, P. Honeine, F. Abdallah, Coordconv-unet: Investigating coordconv for organ segmentation, IRBM 42 (2021) 415–423.
- [48] N. Codella, D. Gutman, M. Celebi, B. Helba, M. Marchetti, S. Dusza, A. Kalloo, N. Liopyris, K. and Mishra, H. Kittler, et al., Skin lesion analysis toward melanoma detection: A challenge at the 2017 international symposium on biomedical imaging (isbi), hosted by the international skin imaging collaboration (isic), 2018 IEEE 15th international symposium on biomedical imaging (ISBI 2018) (2018) 168–172.
- [49] N. Codella, V. Rotemberg, P. Tschandl, M. Celebi, S. Dusza, D. Gutman, B. Helba, A. Kalloo, K. Liopyris, M. Marchetti, et al., Skin lesion analysis toward melanoma detection 2018: A challenge hosted by the international skin imaging collaboration (isic), arXiv preprint arXiv:1902.03368 (2019).